Tectonophysics 733 (2018) 273–295

Contents lists available at ScienceDirect

Tectonophysics

journal homepage: www.elsevier.com/locate/tecto

A comparison between rate-and-state friction and microphysical models, based on numerical simulations of fault slip

M.P.A. van den Ende[a,*], J. Chen[a], J.-P. Ampuero[b], A.R. Niemeijer[a]

[a] High Pressure and Temperature Laboratory, Department of Earth Sciences, Utrecht University, The Netherlands
[b] Seismological Laboratory, California Institute of Technology, Pasadena, CA, USA

ARTICLE INFO

Keywords:
Earthquake nucleation
Dynamic rupture propagation
Microphysics
Rate-and-state friction

ABSTRACT

Rate-and-state friction (RSF) is commonly used for the characterisation of laboratory friction experiments, such as velocity-step tests. However, the RSF framework provides little physical basis for the extrapolation of these results to the scales and conditions of natural fault systems, and so open questions remain regarding the applicability of the experimentally obtained RSF parameters for predicting seismic cycle transients. As an alternative to classical RSF, microphysics-based models offer means for interpreting laboratory and field observations, but are generally over-simplified with respect to heterogeneous natural systems. In order to bridge the temporal and spatial gap between the laboratory and nature, we have implemented existing microphysical model formulations into an earthquake cycle simulator. Through this numerical framework, we make a direct comparison between simulations exhibiting RSF-controlled fault rheology, and simulations in which the fault rheology is dictated by the microphysical model. Even though the input parameters for the RSF simulation are directly derived from the microphysical model, the microphysics-based simulations produce significantly smaller seismic event sizes than the RSF-based simulation, and suggest a more stable fault slip behaviour. Our results reveal fundamental limitations in using classical rate-and-state friction for the extrapolation of laboratory results. The microphysics-based approach offers a more complete framework in this respect, and may be used for a more detailed study of the seismic cycle in relation to material properties and fault zone pressure-temperature conditions.

1. Introduction

The destructive potential of earthquakes poses major societal challenges, and thus calls for a deep understanding of the underlying mechanics for reliable seismic hazard assessment. In order to better apprehend both natural and induced seismicity, much laboratory work is aimed at characterising the frictional behaviour of rock materials, or of their analogues. The microstructures produced by laboratory deformation tests can then be compared with those retrieved from natural outcrops to augment the interpretation of the laboratory results. Both the macroscopic mechanical behaviour and the formation of the fault zone microstructure are controlled by the micro-scale deformation mechanisms that accommodate (shear) strain (Niemeijer and Spiers, 2006). Thus, extrapolation of laboratory results to the spatial and temporal scales of natural faults may be facilitated through the study and quantification of micro-scale processes, provided that they operate within natural faults at the relevant pressure and temperature conditions.

Most commonly, the laboratory friction data are described in the framework of rate-and-state friction (RSF), which provides empirical relations between the measured coefficient of friction (μ), rate of deformation (V), and "state"(θ). While some variations exist, the most widely used functional form reads (Dieterich, 1979; Ruina, 1983):

$$\mu(V, \theta) = \mu^* + a \ln\left(\frac{V}{V^*}\right) + b \ln\left(\frac{V^*\theta}{D_c}\right) \quad (1)$$

where μ^* is a reference coefficient of friction measured at sliding velocity V^*. The parameters a and b are proportionality constants for the magnitudes of the instantaneous "direct" and time-dependent "evolution" effects, respectively, and are thought to represent material properties. The characteristic slip distance D_c controls the slip distance over which the evolution towards the new steady-state takes place. The evolution of the state parameter θ is formulated either by the "ageing law"(Eq. (2a); Dieterich, 1979) or "slip law"(Eq. (2b); Ruina, 1983):

$$\frac{d\theta}{dt} = 1 - \frac{V\theta}{D_c} \quad (2a)$$

* Corresponding author.
E-mail address: m.p.a.vandenende@uu.nl (M.P.A. van den Ende).

https://doi.org/10.1016/j.tecto.2017.11.040
Received 26 July 2017; Received in revised form 9 November 2017; Accepted 28 November 2017
Available online 05 December 2017

$$\frac{d\theta}{dt} = -\frac{V\theta}{D_c}\ln\left(\frac{V\theta}{D_c}\right) \quad (2b)$$

At steady-state, both state evolution laws reduce θ to D_c/V, so that the steady-state coefficient of friction can be simply expressed as:

$$\mu_{ss}(V) = \mu^* + (a - b)\ln\left(\frac{V}{V^*}\right) \quad (3)$$

The parameter $(a - b)$ now describes the velocity-dependence of μ at steady-state, with positive values (i.e. $a > b$) resulting in velocity-strengthening, and negative values resulting in velocity-weakening behaviour. It has been demonstrated by Ruina (1983) that a material characterised by a negative $(a - b)$ is prone to frictional instabilities, i.e. stick-slip behaviour, and thus it is assumed that seismogenic fault segments exhibit a negative $(a - b)$.

Combined with Eq. (2), Eq. (1) yields a versatile relation that describes a wide range of laboratory data (e.g. Blanpied et al., 1998; He et al., 2016; Leeman et al., 2015; Marone, 1998). Numerous experimental studies report values of RSF parameters for natural (Boulton et al., 2012, 2014; Carpenter et al., 2009, 2014; Collettini et al., 2011; Niemeijer and Vissers, 2014; Niemeijer et al., 2016; Sawai et al., 2016; Tesei et al., 2014) and synthetic gouges (Blanpied et al., 1991, 1995, 1998; Carpenter et al., 2009; Chester, 1994; Chester and Higgs, 1992; den Hartog et al., 2012, 2013; He et al., 2007, 2013; Ito and Ikari, 2015; Saffer and Marone, 2003; Verberne et al., 2015), as well as for analogue materials (Buijze et al., 2017; Leeman et al., 2015; Takahashi et al., 2017). The RSF parameters (a, b, and D_c) obtained from laboratory experiments then serve as an input for numerical modelling studies (e.g. Kaneko et al., 2017; Lapusta and Rice, 2003). Typical values for $(a - b)$ reported by experimental studies lie in the range of $\pm 10^{-3}$-10^{-2} (e.g. Boulton et al., 2014; Chester, 1994; He et al., 2007; den Hartog et al., 2012, 2013; Scholz, 2002), although much larger values have been reported up to $+0.15$ by Blanpied et al. (1998), and down to -0.05 by Takahashi et al. (2017) and -0.2 by Buijze et al. (2017). Most of these experimental studies reveal a dependence of the obtained RSF parameters on experimental conditions, including (but not limited to) ambient temperature (Blanpied et al., 1991, 1995, 1998; Chester and Higgs, 1992; den Hartog et al., 2012, 2013; He et al., 2007, 2013; Sawai et al., 2016; Verberne et al., 2015), deformation rate (Carpenter et al., 2016; Collettini et al., 2011; den Hartog et al., 2012; Reinen et al., 1992; Tesei et al., 2014), imposed normal stress (Carpenter et al., 2016; Chester, 1994; Sawai et al., 2016), and pore fluid chemistry (Feucht and Logan, 1990; Hunfeld et al., 2017). When considering a wide range of conditions, covered either fully or partially by each of the aforementioned studies, at least three regimes of velocity-dependence of friction can be observed: at low imposed velocities or high ambient temperatures, the gouge material is often found to exhibit velocity-strengthening behaviour with very high positive values of $(a - b)$ as compared to room temperature conditions (e.g. Blanpied et al., 1998; den Hartog et al., 2012), which has been attributed to ductile or plastic creep (Bos and Spiers, 2002; Noda and Shimamoto, 2010; Reinen et al., 1992; Shimamoto, 1986). At intermediate velocities and temperatures, a transition is made into the velocity-weakening regime with $(a - b) < 0$ (e.g. Blanpied et al., 1998; den Hartog et al., 2012; He et al., 2007), characterised by an increasingly more porous and cataclastic microstructure with increasing sliding velocity (Niemeijer and Spiers, 2006). At high velocities or low temperatures, most gouges again exhibit (mildly) velocity-strengthening friction (e.g. He et al., 2007; Marone et al., 1990; Sawai et al., 2016). Finally, several mechanisms have been identified to cause intense frictional weakening at coseismic slip velocities, which could be interpreted as an additional stage of velocity-weakening in the dynamic regime (see Niemeijer et al., 2012; Tullis, 2007, and references therein). The full range of frictional behaviour that is expected to feature on large faults during the seismic cycle, from low-velocity creep to high-velocity dynamic weakening, is reported for halite by Buijze et al. (2017).

In spite of its inherent versatility, classical rate-and-state friction is not able to capture the full extent of frictional behaviour observed in experiments with a single set of parameters. To account for transitions from velocity-strengthening to -weakening (and vice versa), the classical RSF framework has been modified and extended, for example by coupling of the RSF equations with a creep law (Noda, 2016; Noda and Shimamoto, 2010, 2012), or by introduction of a cut-off velocity (e.g. Okubo, 1989; Shibazaki and Iio, 2003). However, the modified RSF relations remain (mostly) empirical and do not offer a physical explanation for many experimental observations, such as the dependence of RSF parameters on the imposed normal stress, or the presence of a reactive fluid. This inhibits the extrapolation of laboratory results to the spatial- and temporal scales of natural faults. Particularly, since most experimental work focusses on the near-steady state behaviour of faults, it can be questioned whether or not the RSF parameters derived from these experiments can be applied to describe the full seismic cycle, including all of its transient features observed in nature.

As an alternative approach, microphysics-based models may provide us with a more solid basis for the extrapolation of laboratory results, since the dependence of their input parameters on thermodynamic quantities (temperature, pressure, state of stress) can be either predicted or constrained by laboratory and field observations. In recent years, several attempts have been made to derive such microphysical models and to use these to explain the seismogenic potential of faults (den Hartog and Spiers, 2014; Ikari et al., 2016; Noda, 2008; Perfettini and Molinari, 2017; Putelat et al., 2011; Sleep, 2005, and others). The microphysical models hold a major advantage over empirical models, in that their assumptions have a clear physical interpretation, so that the validity of the assumptions, and the applicability and limitations of the model can be evaluated. Moreover, some microphysical models provide a coupling with experimental or field observations through predictions pertaining the microstructure, in addition to a predicted macro-mechanical response (e.g. den Hartog and Spiers, 2014; Niemeijer and Spiers, 2007). However, the constitutive relations given by microphysical models are often highly simplified in order to arrive at closed-form expressions, and generally do not match the heterogeneity and geometrical complexity of natural faults.

To address the issue of up-scaling, numerical seismic simulators are commonly employed. These numerical frameworks often handle non-uniform distributions of fault properties, fault slip, and stress, and are used for studying the non-steady state behaviour of natural faults. Examples include fully- and quasi-dynamic rupture propagation (Thomas et al., 2014; Zheng and Rice, 1998), the statistics and scaling of (sub)seismic slip events (Hillers et al., 2007; Luo et al., 2017a), and nucleation of both slow and fast events (Ariyoshi et al., 2012; Hawthorne and Rubin, 2013; Kaneko et al., 2017; Luo and Ampuero, this issue; Shibazaki and Iio, 2003). But while the numerical simulators offer the desired complexity in terms of fault heterogeneity and geometry, they are typically based on rate-and-state friction, and are therefore limited by the aforesaid problem of extrapolation of RSF parameters beyond the scales and condition of the laboratory. Moreover, the RSF model input parameters are typically imposed as time-constant values, which may not necessarily be accurate, as these parameters may evolve with slip (Mair and Marone, 1999; Scuderi et al., 2017; Urata et al., 2017), or depend on slip velocity (Collettini et al., 2011; den Hartog et al., 2012; Reinen et al., 1992).

In an attempt to bridge the gap between the laboratory and nature, we have implemented the microphysical model formulations of Niemeijer and Spiers (2007) and Chen and Spiers (2016) ("CNS") into the seismic cycle simulator QDYN (Luo et al., 2017a,b), which we will detail in this work. As a test-case, we analyse the behaviour of a crustal strike-slip fault, similar to the work of Tse and Rice (1986) and Lapusta and Rice (2003). We compare the outcomes of the microphysics-based model with the results from classical rate-and-state friction simulations, and discuss the differences between the two within a framework of upscaling laboratory results to nature. The simulations reveal that the implementation of the microphysical models results in characteristic

fault slip behaviour previously ascribed to rate-and-state friction. However, the comparison between the rate-and-state based model and the microphysics-based model strongly suggests that the CNS-governed fault rheology cannot accurately be represented by classical rate-and-state friction. This implies that typical laboratory tests aimed at deriving RSF parameters may not be representative for the seismic cycle behaviour of faults exhibiting CNS microphysics (pressure solution and granular flow). The implementation of a microphysical model now offers an interpretation of simulation results in terms of material properties and thermodynamic quantities. This invites for future research into the controlling mechanisms of earthquake nucleation and rupture propagation, through the study of the underlying micro-scale processes.

2. Microphysical framework

For the implementation of the micro-scale physics, we have chosen the formulations of Niemeijer and Spiers (2007) and Chen and Spiers (2016) (from here on referred to as "CNS model"), which describe the evolution of the frictional strength and microstructural state of well-matured fault gouges. The term "friction" is here used in a general sense to describe the shear resistance of a fault. Even though superficially the functional form of the CNS constitutive relations shares little resemblance with the classical rate-and-state framework, the CNS model predictions of the transient frictional response to typical laboratory procedures (such as velocity-step tests and slide-hold-slide tests) very closely match characteristic RSF behaviour (Chen and Spiers, 2016; Chen et al., 2017). Furthermore, trends in experimental data for principal slip zone gouges of the Alpine Fault (obtained by Niemeijer et al., 2016) can be accurately predicted by the CNS model (Chen et al., 2017, their Fig. 13), which provides some confidence that the physical processes relevant for earthquake nucleation in natural fault zones are well captured by the CNS model. The main concepts of the CNS model are summarised below.

The idealised geometry that the CNS model considers is that of a uniform layer of granular gouge, characterised by a nominal grain size d, porosity ϕ, and total thickness L (see Fig. 2). Optionally, the degree of localisation can be defined as a fraction λ of the total thickness L, which allows for a decomposition of the gouge body into a domain of active shear deformation (the shear band), and a spectator domain (the bulk). For the purpose of this study, we take $\lambda = 1$, which is equivalent to saying that the entire gouge layer participates in accommodation of the imposed shear strain (see Chen and Spiers, 2016). A representative elementary volume defined by the above microstructural description is subjected to a constant effective normal stress σ, and shear deformation rate V_{imp} (units m/s). The deformation imposed by these boundary conditions is then accommodated within the body of the gouge by the parallel operation of granular flow (grain sliding) and a thermally-activated, time-dependent deformation mechanism. The strain rate contributions of these micro-scale deformation mechanisms as a function of the state of stress and gouge microstructural state can then be described by their respective constitutive relations, so that ultimately the shear resistance of the fault results from a combination of ductile creep and dilatant friction. In this work, we focus on the interplay between granular flow and intergranular pressure solution, a diffusive mass transfer mechanism that is commonly observed to operate in crustal faults (Chester et al., 1993; Holdsworth et al., 2011; Imber et al., 2008). Other deformation mechanisms (stress corrosion cracking, dislocation creep, etc.) could be incorporated in a similar fashion.

For pressure solution, we adopt a linearised flow law for dissolution controlled pressure solution creep (Niemeijer et al., 2002; Pluymakers and Spiers, 2014):

$$\dot{\gamma}_{ps} = A_t \frac{I_s \Omega}{RT} \frac{\tau}{d} f_1(\phi) \tag{4a}$$

$$\dot{\varepsilon}_{ps} = A_n \frac{I_s \Omega}{RT} \frac{\sigma}{d} f_2(\phi) \tag{4b}$$

In these expressions, $\dot{\gamma}_{ps}$ and $\dot{\varepsilon}_{ps}$ denote the pressure solution strain rates tangential and normal to fault plane, i.e. the simple shear and uniaxial normal components of the strain rate tensor, respectively (taking compaction as $\dot{\varepsilon} > 0$). I_s denotes the (temperature-dependent) dissolution rate constant, Ω the molar volume of the solid phase, R the universal gas constant, T the absolute temperature, τ and σ are the macroscopic shear and effective normal stress, respectively (compression taken positive), and A_x is a geometric constant for the tangential (t) and normal (n) components. In this work, it is assumed that $A_t = A_n = A$, as the exact value of A_t is currently not precisely known. The evolution of the average grain contact stress is described by the porosity function $f_i(\phi)$ (Spiers et al., 2004). For dissolution controlled pressure solution, this function takes the form (Pluymakers and Spiers, 2014):

$$f_1(\phi) = \frac{\phi_c}{\phi_c - \phi} \tag{5}$$

where ϕ_c is the maximum attainable (critical state) porosity of the dry gouge material (Niemeijer and Spiers, 2007; Paterson, 1995). It has been reported that this porosity function overestimates the compaction rates of low porosity aggregates, and does not accurately describe the evolution of pressure solution strain rate with porosity for $\phi < 20\%$ (Niemeijer et al., 2002; Schutjens, 1991a). van Noort et al. (2008a) suggested that the discrepancy between analytical models and experimental compaction data at low porosities can be explained by considering surface energy-driven growth of grain contact asperities (i.e. grain boundary healing). While it is possible to include this mechanism into the above formulations, we chose to approximate this behaviour by modifying the porosity function given by Eq. (5) into:

$$f_2(\phi) = \frac{\phi - \phi_0}{\phi_c - \phi} \tag{6}$$

Here, ϕ_0 is a lower cut-off porosity which corresponds to the terminal porosity observed in experiments (Niemeijer et al., 2002; Schutjens, 1991a), which could be taken as the percolation threshold for an interconnected pore network (van der Marck, 1996). By using the above relation, we can approximate the rapid decay in strain rates with decreasing porosity observed in compaction experiments, without explicitly considering additional mechanisms that would otherwise complexify the implementation. As ϕ approaches ϕ_0, $\dot{\varepsilon}_{ps}$ reduces to 0, i.e. compaction by pressure solution asymptotically approaches zero, preventing $\phi \leq \phi_0$. Note that Eq. (6) is only used for the densification of the gouge, i.e. compaction parallel to the fault plane normal (Eq. (4b)). Since ductile shear creep by pressure solution (Eq. (4a)) does not cause porosity reduction and may also operate at $\phi = \phi_0$, it is likely more appropriate to describe this process using the originally proposed porosity function (Eq. (5)).

The constitutive relations for granular flow are provided by Chen and Spiers (2016), and read:

$$\dot{\gamma}_{gr} = \dot{\gamma}^*_{gr} \exp\left(\frac{\tau [1 - \tilde{\mu}^* \tan\psi] - \sigma [\tilde{\mu}^* + \tan\psi]}{\tilde{a} [\sigma + \tau \tan\psi]} \right) \tag{7a}$$

$$\dot{\varepsilon}_{gr} = -\tan\psi \dot{\gamma}_{gr} \tag{7b}$$

Here, the $\dot{\gamma}_{gr}$ and $\dot{\varepsilon}_{gr}$ denote the granular flow strain rates tangential and normal to fault plane, respectively, and $\tan\psi$ denotes the average dilatation angle, which can accordingly be written as $\tan\psi = 2H(\phi_c - \phi)$, H being a geometric constant (Niemeijer and Spiers, 2007; Paterson,

1995). The geometric constant H primarily depends on the grain shape and grain size distribution of the gouge, controlling the amount of dilatation that is involved in neighbour swapping and grain sliding. The magnitude of H can be predicted based on theoretical considerations, which would yield a value in the range $1/\sqrt{3}$ to $\sqrt{3}$ in 2D (Niemeijer and Spiers, 2007), or can be inferred from biaxial or triaxial deformation tests on sands and soils, which gives values in the range of 0.4 to 0.6 for dense sands (assuming a critical state porosity $\phi_c = 0.4$) (see Vermeer and De Borst, 1984). However, putting tight constrains on the exact value of H is challenging, particularly when grain comminution operates during sliding, by which H would likely evolve. Dedicated laboratory tests and numerical simulations (e.g. employing the Discrete Element Method) could constrain this parameter further for grain size distributions relevant for natural gouges.

The micro-scale coefficient of friction of the individual grain contacts has a logarithmic velocity-dependence, which is given as $\tilde{\mu} = \tilde{\mu}^* + \tilde{a}\ln(\dot{\gamma}_{gr}/\dot{\gamma}^*_{gr})$, with $\tilde{\mu}^*$ being the coefficient of friction at a reference grain sliding rate $\dot{\gamma}^*_{gr}$. In this form, the velocity-dependence of $\tilde{\mu}$ closely resembles the direct effect in the classical rate-and-state formulation and asperity-creep based microphysical models (e.g. Nakatani, 2001; Rice et al., 2001). Notwithstanding this resemblance, the approach for deriving this relation is somewhat different, in that an atomic-scale jump process is considered to constitute the frictional slip at the nanometre scale of two grain contact asperities, rather than assuming deformation of an asperity through a dislocation glide or creep mechanism. Ultimately, the coefficient of logarithmic rate-dependence $\tilde{a}$ can be reduced to (Chen and Spiers, 2016):

$$\tilde{a} = \frac{RT}{\sigma_a \Omega_a} \tag{8}$$

where σ_a is the effective normal stress supported by grain contact asperities. Ω_a can be interpreted as an activation volume for the atomic-scale jump process. Classically, σ_a is taken to represent the elastic-plastic yield strength of the asperities, approximated by the material indentation hardness (e.g. Ikari et al., 2016; Rice et al., 2001). However, for rock materials undergoing fluid-rock interactions, it has been convincingly demonstrated that the size of contact asperities (or 'islands') is controlled by dissolution-precipitation processes (Beeler and Hickman, 2015; Hickman and Evans, 1991; Renard et al., 2012; Schutjens and Spiers, 1999), hence it is unlikely that σ_a of fluid-saturated gouges can be represented by the indentation hardness of a material. Furthermore, the porosity of a gouge exerts strong control on the average stress supported by each grain contact, rendering σ_a dependent on gouge porosity, strictly speaking (Chen and Spiers, 2016). However, during accelerating fault slip the porosity of the gouge quickly approaches the critical state porosity ϕ_c, after which the gouge porosity remains approximately constant. Additionally, since frictional heating is not considered in this work it would be unjustified to consider the effect of porosity, while ignoring the effect of frictional heat on the magnitude of $\tilde{a}$ during rapid slip. Thus, we assume for simplicity that σ_a increases proportionally to σ, thereby ignoring contributions from the gouge porosity in elevating the average grain contact stress. Even though the physical meaning and constituents of Ω_a are clear (see Chen and Spiers, 2016, for derivation and discussion), it remains non-trivial to predict its exact magnitude purely based on physical considerations. However, under the first-order assumption that $\sigma_a \propto \sigma$, $\tilde{a}$ can be written as:

$$\tilde{a} = \tilde{a}^* \frac{T}{T^*}\frac{\sigma^*}{\sigma} \tag{9}$$

where $\tilde{a}^*$ is an experimentally determined value measured at reference temperature T^* and normal stress σ^*. Interestingly, this makes the rate-and-state equivalent "direct effect" not only temperature-dependent, as is often assumed (Ikari et al., 2016; Nakatani, 2001; Rice et al., 2001), but also stress-dependent. As derived by Chen et al. (2017), the equivalent RSF parameter a following a small velocity step can be approximated as $a \approx \tilde{a}(1 + \tan\psi_{ss}^2)$, where $\tan\psi_{ss}$ is evaluated at the steady-state porosity prior to the velocity step. Hence, there exists a potential for $\tilde{a}$ to decrease with depth, rather than increase when only a temperature proportionality is assumed (e.g. Lapusta and Rice, 2003; Tse and Rice, 1986), although a small contribution from $\tan\psi_{ss}$ needs to be considered to be more exact.

Having established the constitutive relations for pressure solution and granular flow, we now follow Chen and Spiers (2016) to use simple kinematic relations that yield a set of differential equations describing the evolution of the macroscopic shear stress and bulk gouge porosity:

$$\frac{d\tau}{dt} = k(V_{imp} - L[\dot{\gamma}_{gr} + \dot{\gamma}_{ps}]) \tag{10a}$$

$$\frac{d\phi}{dt} = -(1 - \phi)(\dot{\varepsilon}_{gr} + \dot{\varepsilon}_{ps}) \tag{10b}$$

in which k is the effective stiffness (units: Pa m^{-1}) of the fault zone and surrounding medium. The instantaneous fault slip velocity V results from addition of the strain rates of granular flow and pressure solution, i.e. $V = L(\dot{\gamma}_{gr} + \dot{\gamma}_{ps})$. What the above formulations show, is that the CNS model is modular in its design, in the sense that different (micro)physical processes can be readily incorporated within the existing model formulations. When additional deformation mechanisms are to be considered, their contributions to the total strain rate in the normal and shear directions can be simply appended in Eq. (10). This offers opportunities for modelling very specific fault zone conditions and rheologies.

When the above coupled differential equations are solved for the steady-state ($\dot{\tau} = \dot{\phi} = 0$), three distinct deformation regimes emerge:

- When $\dot{\gamma}_{gr} \ll \dot{\gamma}_{ps}$ and $\dot{\varepsilon}_{gr} \ll \dot{\varepsilon}_{ps}$, the imposed deformation is fully accommodated by pressure solution creep. Since $\dot{\varepsilon}_{ps} \gg \dot{\varepsilon}_{gr}$ in this regime, compaction continues until ϕ approaches ϕ_0, so that strain is accommodated at near-zero porosity. This velocity-strengthening regime is analogous to the ductile or plastic creep regimes recognised in previous studies (Noda and Shimamoto, 2010; Reinen et al., 1992; Tullis and Yund, 1987; Verberne et al., 2017), and is characterised by a dense, mylonitic gouge structure (Bos et al., 2000; Sibson, 1977; Takahashi et al., 2017; Zhang and He, 2016).
- When $\dot{\gamma}_{gr}$ is of similar order as $\dot{\gamma}_{ps}$, the competition between dilatant granular flow and compaction by pressure solution results in a dynamic steady-state porosity. This steady-state porosity arises from the adverse dependencies of $\dot{\varepsilon}_{ps}$ and $\dot{\varepsilon}_{gr}$ on ϕ: with increasing ϕ, $\dot{\varepsilon}_{ps}$ increases through $f_2(\phi)$, whereas $\dot{\varepsilon}_{gr}$ decreases through a decreasing value of $\tan\psi$. Hence, at a given magnitude of $\dot{\gamma}_{gr}$, there exists a porosity for which $\dot{\varepsilon}_{ps} = \dot{\varepsilon}_{gr}$ and so $\dot{\phi} = 0$ (defining steady-state). With increasing $\dot{\gamma}_{gr}$, a steady-state is found at increasingly higher values of ϕ, as was also observed in the experiments performed by Niemeijer and Spiers (2006). The strength of the gouge decreases with increasing gouge porosity (i.e. decreasing $\tan\psi$, see Eq. (7a)), hence producing velocity-weakening behaviour (Niemeijer and Spiers, 2007).
- Finally, when $\dot{\gamma}_{gr} \gg \dot{\gamma}_{ps}$, the steady-state porosity asymptotically approaches the critical state porosity ϕ_c, with only little dilatation associated with increasing $\dot{\gamma}_{gr}$. In the absence of changes in gouge strength due to any further increase in porosity, the velocity-dependence of the gouge is controlled by rate-strengthening grain boundary friction. Characteristic microstructures for this regime

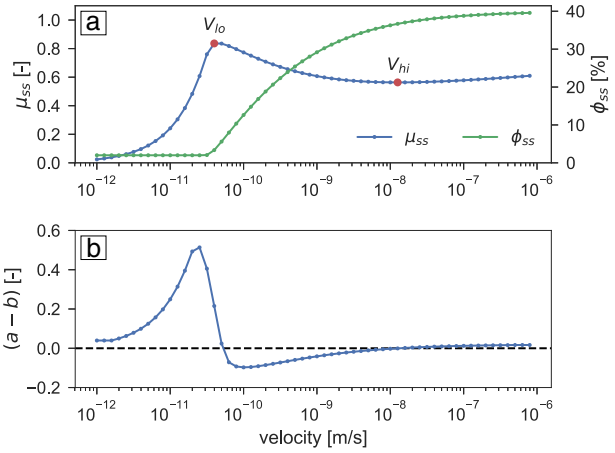

Fig. 1. Velocity-dependence of a) the steady-state coefficient of friction μ_{ss} and porosity ϕ_{ss}, and b) the equivalent value of $(a-b)$. The data was generated for a constant depth of 6 km and $H = 0.5$ (see Section 3.2.1). The points of velocity-neutrality are indicated in panel a) as V_{lo} and V_{hi}.

reveal high porosities and abundant cataclastic features, typical for high-porosity gouges (Niemeijer and Spiers, 2006).

Since at steady-state $\dot{\gamma}_{gr}$ and $\dot{\gamma}_{ps}$ are related through the imposed velocity, the three deformation regimes predicted by the CNS model can be observed experimentally when a sufficiently large range of deformation rates is covered (Buijze et al., 2017; Shimamoto, 1986). The velocity-dependence of the steady-state coefficient of friction μ_{ss} and porosity ϕ_{ss}, as well as corresponding values of $(a-b)$ as predicted by the CNS model are displayed in Fig. 1. At the transition from one deformation regime to the next, the velocity-dependence of the shear strength reaches neutrality, i.e. $(a-b) = 0$ in the RSF formulation. We define the transition velocities V_{lo} for the transition from ductile creep to velocity-weakening, and V_{hi} for the transition from velocity-weakening to velocity-strengthening at high imposed velocities. The absolute values of these transitional velocities are controlled by the relative rates of pressure solution and granular flow, and so depend on the (temperature-dependent) kinetics of pressure solution, nominal grain size, and gouge composition. Thus, the main regimes of deformation shift as a function of temperature, as has also been observed experimentally (Chester and Higgs, 1992; den Hartog et al., 2012; Mitchell et al., 2016; Tullis and Yund, 1987; Zhang and He, 2016).

3. Numerical methods

In essence, Eq. (10) describes the behaviour of a zero-dimensional spring-block. In order to introduce further complexity and to up-scale these relations to natural fault systems, we have implemented the CNS relations into the open-source boundary element code QDYN (**Q**uasi-**DYN**amic earthquake simulator; Luo et al., 2017a,b available at https://github.com/ydluo/qdyn). In the following section, we will describe the relevant details of the implementation of the CNS model into QDYN. For completeness, a concise description of the boundary element method is provided in Appendix A.

3.1. Implementation of the microphysical model

As described in Appendix A, the state of stress acting on each point on the fault is obtained through integration of a system of ordinary differential equations, which includes the time-derivative of the shear stress τ_i on the i-th fault element as:

$$\frac{\mathrm{d}\tau_i}{\mathrm{d}t} = -K_{ij}\left[V_j(t) - V_{imp}\right] - \eta\frac{\mathrm{d}V_i(t)}{\mathrm{d}t} \qquad \text{(A.2 revisited)}$$

where K_{ij} is a stress transfer kernel, and η is a radiation damping term. The total derivative $\mathrm{d}V_i/\mathrm{d}t$ can be decomposed into its partial derivatives as:

$$\frac{\mathrm{d}V_i}{\mathrm{d}t} = \frac{\partial V_i}{\partial \tau}\frac{\mathrm{d}\tau_i}{\mathrm{d}t} + \frac{\partial V_i}{\partial \phi}\frac{\mathrm{d}\phi_i}{\mathrm{d}t} \qquad (11)$$

Substitution of Eq. (11) into Eq. (A.2) and rearrangement now gives the final system of ordinary differential equations for the CNS formulation:

$$\frac{\mathrm{d}\tau_i}{\mathrm{d}t} = \frac{-K_{ij}(V_j - V_{imp}) - \eta\frac{\partial V_i}{\partial \phi}\frac{\mathrm{d}\phi_i}{\mathrm{d}t}}{1 + \eta\frac{\partial V_i}{\partial \tau}} \qquad (12a)$$

$$\frac{\mathrm{d}\phi_i}{\mathrm{d}t} = -(1-\phi_i)(\dot{\varepsilon}_{gr,i} + \dot{\varepsilon}_{ps,i}) \qquad (12b)$$

In this form, V_i is calculated for each fault element as $V_i = L_i(\dot{\gamma}_{gr,i} + \dot{\gamma}_{ps,i})$, which yields the following partial derivatives for V:

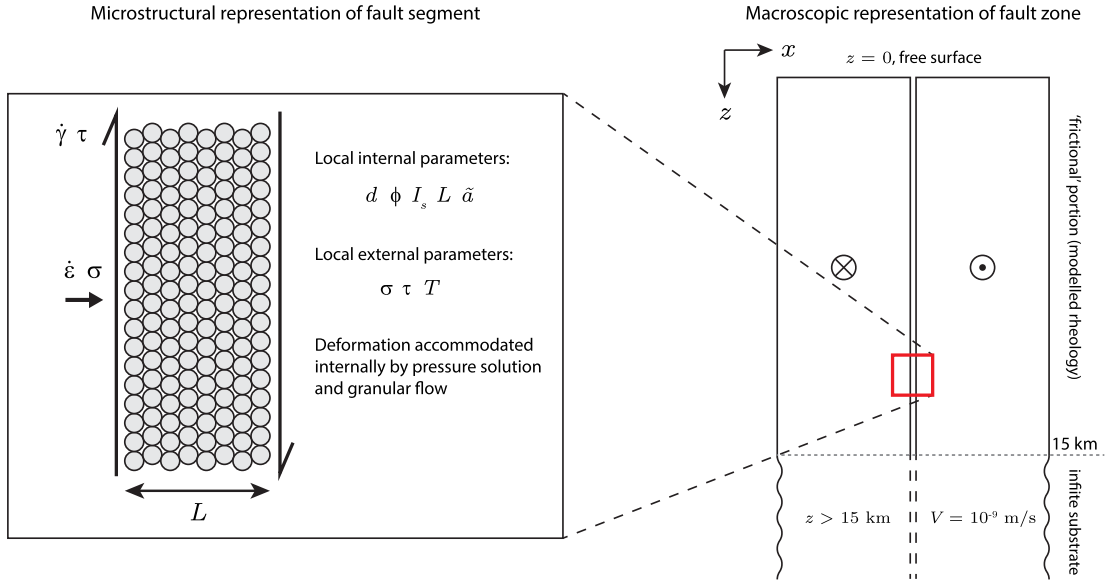

Fig. 2. Geometry and boundary conditions of the model set-up. The micro- and meso-scale (i.e. individual fault segment) rheology of the fault is dicateddictated by the CNS model implementation, following the geometry of Chen and Spiers (2016) (left). At the macro-scale, the fault is represented as a one-dimensional vertical line that is deformed within a two-dimensional elastic medium (right). Note that in this diagram the sense of shear of the microstructural representation does not match that of the macroscopic representation.

$$\frac{\partial V}{\partial \tau} = L\left(A\frac{I_s \Omega}{dRT} f_1(\phi) + \dot{\gamma}_{gr}\left[\frac{1-\tilde{\mu}\tan\psi}{\tilde{a}(\sigma+\tau\tan\psi)}\right]\right) \tag{13a}$$

$$\frac{\partial V}{\partial \phi} = L\left(\frac{\dot{\gamma}_{ps}}{\phi_c - \phi} + \dot{\gamma}_{gr}\left[\frac{2H(\sigma+\tilde{\mu}\tau)}{\tilde{a}(\sigma+\tau\tan\psi)}\right]\right) \tag{13b}$$

This set of equations now describes the rheology of the fault as a function of gouge material properties and microstructural state, and allows for spatio-temporal variations of the controlling parameters. In this way, we are able to predict how the fault frictional behaviour may vary with depth, and may evolve over the life-time of the seismic cycle.

In this work, we define 'steady-state' when $\dot{\tau} = \dot{\phi} = 0$ at V_{imp}. This definition also applies when V_{imp} is systematically varied between simulations, but maintained constant during each simulation, as is done to determine the steady-state shear strength as a function of load-point velocity. 'Transient' behaviour is defined as the mechanical response when $\dot{\tau} \neq 0$ or $\dot{\phi} \neq 0$ for a given fault segment.

3.2. Simulation procedure

3.2.1. Model set-up

As a first test case for the implementation of the CNS model, we set-up a crustal strike-slip model, similar to the work of Tse and Rice (1986), and Lapusta and Rice (2003) (see Fig. 2 for a visualisation of the geometry). A one-dimensional, vertical fault, whose frictional part extends to a depth of 15 km, is embedded within a two-dimensional elastic medium that exhibits a uniform and constant shear modulus of 30 GPa. The fault is then loaded in mode III by a driving velocity of 10^{-9} m/s ($\approx$ 30 mm/yr), which is of similar magnitude as present-day plate velocities. The fault is discretised by 8192 equal-sized segments providing a spatial resolution of 1.8 m, which proves to be sufficient for numerically stable results (see Appendix B). A free surface is simulated by enforcing symmetry across a mirror plane located at the surface (e.g. Lapusta and Rice, 2003).

The type of fault considered here follows broadly the characteristics of a continental fault as described by Chester et al. (1993), exhibiting a single, discrete fault core which internally accommodates all imposed shear displacements, and where off-fault shear strain rates (e.g. by pressure solution creep) are negligible. Other fault architectures, such as described by e.g. Faulkner et al. (2003) and Kimura et al. (2012), incorporate several principal slip zones surrounded by a creeping, phyllosilicate-rich matrix. In the present CNS formulation, such a geometry may be simulated by taking $\lambda < 1$, so that λL corresponds to the (cumulative) thickness of the fault core, and $(1-\lambda)L$ corresponds to the thickness of the surrounding creeping region, where L is taken as the total width of the fault zone (which may not be well-defined). In effect, strain accommodation by the matrix reduces the strain rate imposed onto the fault core, and so has a similar effect as lowering V_{imp}. However, the aim of this work is to compare the CNS model implementation to previous work (e.g. Lapusta and Rice, 2003; Tse and Rice, 1986), motivating a simple fault structure as adopted by these authors.

In order to estimate the depth-dependency of the normal stress acting on the fault, we need to make assumptions regarding the local fluid pressure gradient. Commonly chosen depth-profiles fall into two categories: for simple analytical investigations it is often assumed that the ratio of pore fluid pressure to the total vertical stress is constant with depth, i.e. $\lambda_p = P/\sigma_v = \text{const}$, which results in a linear increase of effective normal stress with depth (i.e $\sigma \propto [1-\lambda_p]\, z$). However, analyses of borehole data (Suppe, 2014) and theoretical considerations (Rice, 1992) suggest that λ_p is not a constant with depth, and that below the fluid retardation depth, P follows a lithostatic trajectory, resulting in a constant effective normal stress below this given depth. An often cited mechanism for supra-hydrostatic pore fluid pressures is disequilibrium compaction (Grauls, 1997; Morency et al., 2007), although the physical basis for this has yet to be fully elucidated. In a fault system that undergoes large fluid permeability changes during the seismic cycle (Lockner et al., 2009; Sibson, 1990), it can be questioned how the effective normal stress evolves over time, and if it can be approximated by a time-constant profile. While the question of fluid pressurisation is an interesting one, we simply adopt the effective stress profile with depth-dependent λ_p of Lapusta and Rice (2003), based on Rice (1992), for easier comparison with previous work, and leave the effects of fluid pressure for future study. The fault zone temperature follows a constant geotherm of 25 K/km, with a surface temperature of 293 K (see Fig. 4a), and is not affected by internal heat production by fault slip (i.e. no frictional heating is considered).

Finally, the CNS model requires a number of assumptions regarding the chemical and microstructural properties of the gouge. We continue to make further simplifications by assuming a uniform and constant nominal grain size, fault zone thickness, and gouge composition. While these simplifications are not required by the CNS model implementation (fault zone structure and heterogeneity can be readily incorporated), it would likely be easier to interpret the model outcomes with fewer variables to consider. We take quartz as a main constituent for the fault zone, representing typical felsic continental upper crust (Chester and Logan, 1987; Kirkpatrick et al., 2013; Power and Tullis, 1989; Sibson, 1977). Quartz has been shown to exhibit dissolution-controlled pressure solution creep at temperatures relevant for the upper crust, ranging from 150 to 600 °C (Dewers and Hajash, 1995; Niemeijer et al., 2002; Schutjens, 1991b). We use the empirical rate equation provided by Rimstidt and Barnes (1980) to interpolate laboratory data of quartz dissolution in pure water as a function of absolute temperature:

$$\log_{10} k_+ = 1.174 + 2.028 \times 10^{-3} T - \frac{4158}{T} \tag{14}$$

The pressure solution kinetic constant I_s is then obtained as $I_s = k_+ \Omega$ (Niemeijer et al., 2002), with Ω being the molar volume of quartz (2.269×10^{-5} m^3/mol). It was noted by van Noort et al. (2008b) that using the above relation may overestimate experimental compaction rates by up to one order of magnitude when dissipation by plastic deformation is neglected. Furthermore, it is known that the presence of certain cations in solution (e.g. Mg^{2+}, Ca^{2+}, Na^{+}, and Ba^{2+}) may catalyse the process of quartz dissolution (Dove, 1999; Rimstidt, 2015). Typical salinities of pore fluids present in fault zones may be higher than those of seawater (e.g. Ohtani et al., 2000; Parry, 1998), which may accelerate quartz dissolution by over two orders of magnitude (Rimstidt, 2015). Moreover, the presence of phyllosilicates, as commonly found in mature fault zones (Collettini et al., 2011; Faulkner et al., 2003), has been convincingly demonstrated to enhance pressure solution creep by accelerating ionic diffusion rates across a grain contact (Hickman and Evans, 1995; Renard et al., 1997). However, for the case of dissolution-controlled pressure solution (as is anticipated for quartz), phyllosilicates such as muscovite may negatively impact creep rates due to the presence of K^{+} and Al^{3+} cations released by these minerals upon dissolution (Iler, 1973; Niemeijer and Spiers, 2002).

While acknowledging these uncertainties regarding the kinetics of pressure solution in quartz, we choose to adopt Eq. (14) and disregard all of the points mentioned above. Instead of attempting to accurately simulate natural faults, we focus on the comparison between the CNS model implementation and classical rate-and-state friction under identical conditions and fault zone properties. To better constrain the kinetics of pressure solution in quartz gouges, more experimental work is needed on the compaction of quartz aggregates under in-situ fault zone conditions and pore fluid chemistry.

A summary of the model input parameters and their values is given in Table 1.

Table 1
List of frequently used symbols and parameters, and their respective values (if applicable).

Symbol	Description	Value	Units
A	Pressure solution geometric constant	$24/\pi$	–
$\tilde{a}$	Coefficient for logarithmic rate-dependence of $\tilde{\mu}$	–	–
$\tilde{a}^*$	Reference value of $\tilde{a}$	3×10^{-3}	–
c_s	Shear wave speed	3000	m s^{-1}
d	Nominal grain size	10	μm
$\dot{\varepsilon}_{gr}$	Granular flow strain rate	–	s^{-1}
$\dot{\varepsilon}_{ps}$	Pressure solution strain rate	–	s^{-1}
ϕ	Gouge porosity	–	–
ϕ_0	Lowercut-off porosity	0.03	–
ϕ_c	Critical state porosity	0.40	–
G	Shear modulus	30	GPa
$\dot{\gamma}_{gr}$	Granular flow shear strain rate	–	s^{-1}
$\dot{\gamma}^*_{gr}$	Reference $\dot{\gamma}_{gr}$ corresponding with $\tilde{\mu}^*$	3×10^{-9}	s^{-1}
$\dot{\gamma}_{ps}$	Pressure solution shear strain rate	–	s^{-1}
H	Dilatancy geometric constant	0.5 and 0.2	–
η	Radiation damping coefficient	0.5×10^6	Pa s m^{-1}
I_s	Dissolution rate constant (temperature-dependent)	–	m s^{-1}
k	Shear stiffness	–	Pa m^{-1}
L	Thickness of the gouge layer	10^{-2}	m
$\tilde{\mu}$	Grain boundary friction coefficient	–	–
$\tilde{\mu}^*$	Reference grain boundary friction coefficient	0.4	–
Ω	Molar volume	2.269×10^{-5}	m^3 mol^{-1}
R	Universal gas constant	8.3144	J mol^{-1} K^{-1}
V	Fault slip velocity	–	m s^{-1}
V_{imp}	Imposed driving velocity	10^{-9}	m s^{-1}
σ	Effective normal stress	–	Pa
σ^*	Reference σ corresponding with $\tilde{a}^*$	50	MPa
T	Temperature	–	K
T^*	Reference T corresponding with $\tilde{a}^*$	353	K
τ	Shear stress	–	Pa
tanψ	Dilatancy angle	–	–

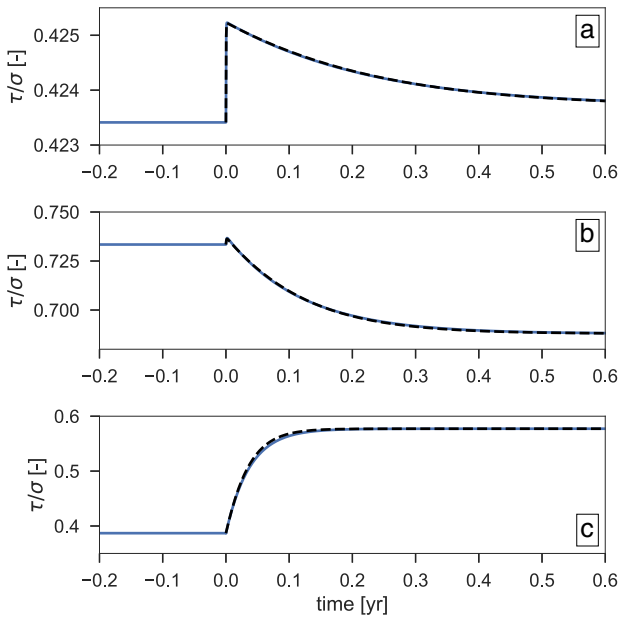

Fig. 3. Representative examples for the velocity-step simulations and corresponding inversion results (black dashed line), for three selected depth intervals (z) with $H = 0.5$. a) $z = 2$ km, $a = 4.5 \times 10^{-3}$, $b = 3.8 \times 10^{-3}$, and $D_c = 7.8$ mm; b) $z = 8$ km, $a = 8.2 \times 10^{-3}$, $b = 1.2 \times 10^{-1}$, and $D_c = 4.4$ mm; c) $z = 11$ km, $a = 4.8 \times 10^{-1}$, $b = 0$, and consequently D_c is undefined.

3.2.2. Comparison of the CNS implementation with rate-and-state friction

In order to compare the CNS implementation with classical rate-and-state friction, we run two crustal strike-slip fault simulations following the model set-up as described in Section 3.2.1 above. In the first simulation (the native CNS simulation), the fault rheology is dictated by the CNS model implementation. In the second (the RSF simulation), we employ classical RSF with a single state parameter, which evolves according to the ageing law (Eq. (2a)). For a direct comparison with the CNS model, the depth-dependent input parameters for this simulation (a, b, and D_c) as predicted by the CNS model need to be estimated. We will refer to these parameters as the 'equivalent' RSF parameters, without implying that these parameters injected into Eq. (1) are unequivocally representative for the CNS model. The equivalent RSF parameters are obtained as follows.

For each given depth interval, a simulation is run in spring-block mode with CNS-governed fault rheology, and with the appropriate input parameters for that specific depth ($\tilde{a}$, I_s, σ, and T). The zero-dimensional, spring-block fault is then loaded at a rate $V_{imp} = 10^{-9}$ m/s with high load-point stiffness until a steady-state is reached, from which the steady-state coefficient of friction is determined as $\mu_{ss} = \tau_{ss}/\sigma$. An additional simulation is run in which a velocity-step test is simulated. In this simulation, the fault is deformed at a rate $V_0 = e^{-0.2} V_{imp}$ until steady-state is reached, followed by an instantaneous step in load-point velocity to $V_1 = e^{0.2} V_{imp}$. The simulation is stopped when the new steady-state is attained. The equivalent rate-and-state parameters are obtained from inversion of Eq. (1) with the ageing state evolution law (Eq. (2a); Reinen and Weeks, 1993) for the transient friction data resulting from this simulation, which is performed by the Trust Region Reflective algorithm (Branch et al., 1999). In the simulated depth intervals where strain is fully accommodated by ductile creep, the steady-state porosity remains near $\phi_{ss} = \phi_0$, which is maintained upon a velocity-step. In these cases, no evolution effect is observed, and so the frictional response is best modelled with $b = 0$. The value of D_c for $b = 0$ is hence undefined and can therefore be arbitrarily chosen without further consequences for the RSF simulations. For depth intervals that exhibit $b \neq 0$ (i.e. where granular flow is significant), D_c results from the

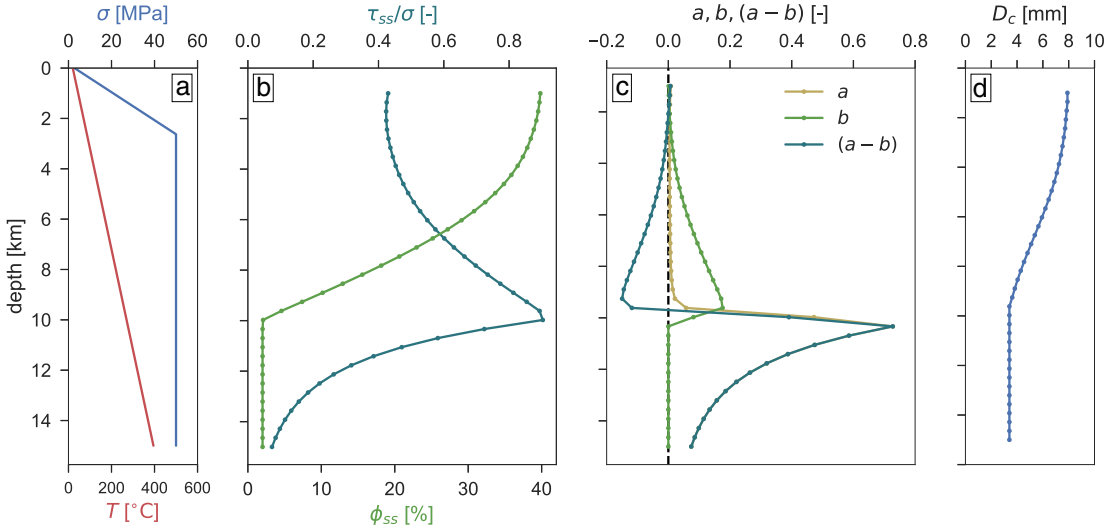

Fig. 4. Depth profiles of steady-state parameters for the model fault for $H = 0.5$, determined at $V = 10^{-9}$ m/s. a) Effective normal stress σ and temperature T; b) Steady-state coefficient of friction μ_{ss} and porosity ϕ_{ss}; c) Equivalent rate-and-state friction parameters a, b, and $(a - b)$. At depths > 10 km, $b = 0$ so that the curve of a overlaps with that of $(a - b)$; d) Equivalent rate-and-state parameter D_c.

inversion procedure. Since the equivalent RSF parameters are velocity-dependent (Chen et al., 2017), the velocity-step size needs to be small for accurate determination of the CNS equivalent RSF parameters, hence our chosen velocity-step size is small compared to most laboratory tests (typically one order in magnitude; Marone et al., 1990; Niemeijer and Spiers, 2006). Furthermore, owing to this velocity-dependence of the equivalent RSF parameters, the velocity at which a, b, and D_c are evaluated is of great importance. In the simulations described in this section, we have chosen to evaluate the equivalent RSF parameters at the load-point velocity, following analytical treatments of frictional instabilities in the RSF framework (e.g. Rice and Ruina, 1983).

The above procedure is repeated for 40 different depth intervals to obtain the depth-dependence of a, b, and D_c as resulting from the CNS model implementation. Representative simulation and inversion results at depth intervals of 2, 8, and 11 km are presented in Fig. 3. Since the crustal fault simulations that employ RSF require a spatial resolution that is much higher than is provided by these 40 depth intervals, the data set is resampled to the required resolution by linear interpolation, and is gently smoothed by a moving-mean filter to prevent steep gradients in the parameters. The equivalent RSF parameters then serve as an input for the RSF simulation, and should provide a direct comparison between the classical RSF and native CNS simulations. The adopted procedure also reflects typical laboratory testing procedures, in which near-steady state velocity-step tests are performed (ideally at in-situ fault zone conditions). It can be questioned whether or not these steady-state laboratory measurements of the RSF parameters can be applied to the seismic cycle, during which deformation occurs far from steady-state. Comparison between the RSF and CNS simulations could provide new insights into this problem, as the CNS model does not require steady-state rheological parameters.

4. Results

4.1. Steady-state behaviour

It is instructive to first consider the steady-state behaviour of the CNS-controlled model fault, i.e. the predicted rheology at $V = V_{imp}$. From the spring-block simulations described in Section 3.2.2, we obtain the steady-state coefficient of friction $\mu_{ss} = \tau_{ss}/\sigma$ (Fig. 4b) and the equivalent RSF parameters a, b, $(a - b)$ (Fig. 4c), and D_c (Fig. 4d).

The profile of $(a - b)$ in Fig. 4c suggests the existence of a seismogenic depth interval (i.e. potentially unstable region of the crust) between 3 and 10 km depth. Shallow depths < 3 km are characterised by mild velocity-strengthening friction due to cataclastic granular flow, consistent with laboratory tests and seismological observations (Marone and Scholz, 1988; Marone et al., 1990). Furthermore, below the depth of 10 km, a region of strong velocity-strengthening (large positive $(a - b)$) emerges, which could be interpreted as defining the brittle-ductile transition as in the classical models of crustal rheology (Sibson, 1982). Note, however, that these results are specific to a given load-point velocity of $V_{imp} = 10^{-9}$ m/s, as both μ_{ss} and equivalent $(a - b)$ are velocity-dependent in the CNS formulation (Chen and Spiers, 2016). Hence, the depth of the seismogenic zone and the brittle-ductile transition *sensu stricto* cannot directly be inferred based on the steady-state behaviour at a single slip velocity, as the fault slip velocity likely varies by over 10 orders of magnitude between the inter- and coseismic phases of the seismic cycle (going from $V \ll V_{imp} = 10^{-9}$ m/s during the interseismic phase to $V \approx 1$ m/s during the coseismic phase). This has important implications for the depth of earthquake nucleation and the direction of dynamic rupture propagation, as we shall demonstrate later.

Within the 'brittle' region, characterised mostly by velocity-weakening at 10^{-9} m/s (upper 10 km), the depth-dependence of the parameter b strongly controls the overall velocity-dependence of the fault, while the parameter a remains relatively small and near-constant. The large magnitude of b (up to 0.18) is not commonly observed in laboratory experiments, where typical values of the order of 10^{-3} to 10^{-2} are found (e.g. Marone et al., 1990; Tesei et al., 2014). However, many of these experiments are conducted at relatively low temperature conditions, and relatively high deformation rates (in the range of 1-100 1–100 μm/s). It has been observed that fluid-rock interactions increase the magnitude of b (Blanpied et al., 1998; He et al., 2016), and so it is likely that b assumes larger values in regions of the crust where fluid-rock interactions occur at appreciable rates. In the limit of an infinitesimally small step-wise velocity perturbation, the value of b as predicted by the CNS model can be approximated as $b \approx H(\phi_c - \phi_{ss})(1 + \tilde{\mu}^2)$, where ϕ_{ss} is the steady-state gouge porosity (Chen et al., 2017). This relation shows that b is expected to increase with decreasing steady-state porosity, which is achieved through time-dependent compaction by, in this case, pressure solution creep. The maximum value of b is attained when $\phi_{ss} \approx \phi_0$ (as is found at the base of the seismogenic zone) for which $b \approx H(\phi_c - \phi_0)(1 + \tilde{\mu}^2) = 0.21$. This analytical approximation corresponds well to the value obtained from

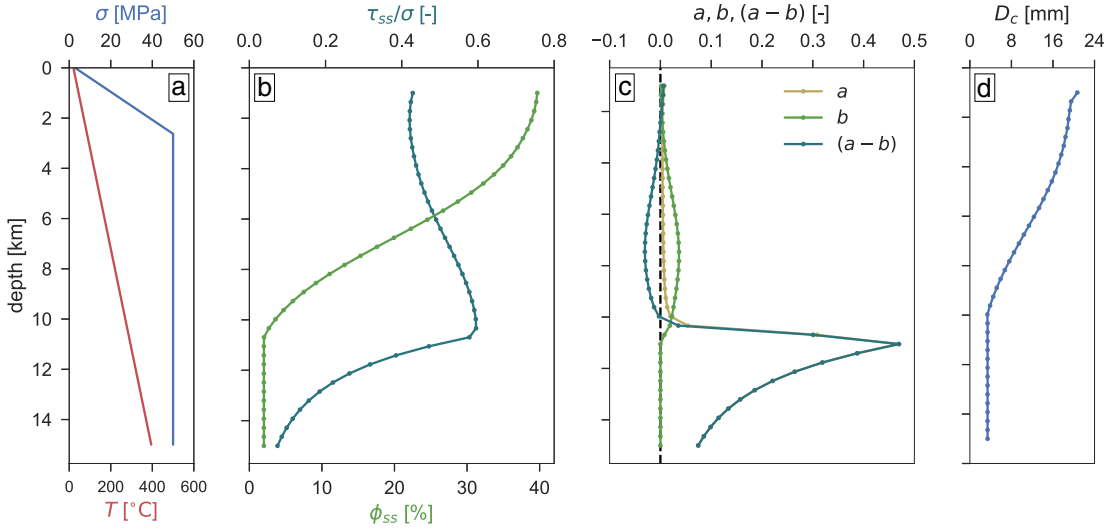

Fig. 5. Depth profiles of steady-state parameters for the model fault for $H = 0.2$, determined at $V = 10^{-9}$ m/s. a) Effective normal stress σ and temperature T; b) Steady-state coefficient of friction μ_{ss} and porosity ϕ_{ss}; c) Equivalent rate-and-state friction parameters a, b, and $(a - b)$. At depths > 10 km, $b = 0$ so that the curve of a overlaps with that of $(a - b)$; d) Equivalent rate-and-state parameter D_c. Note the use of different horizontal axis scales from Fig. 4.

the velocity-step simulations. Other mechanisms that may strongly affect the experimentally measured value of $(a - b)$ include localisation and grain comminution, which are commonly observed in experiments exhibiting velocity-weakening behaviour (Takahashi et al., 2017). These mechanisms are at present not included in the CNS model formulation, and should be considered in future studies.

The large magnitude of $(a - b)$ down to -0.15 poses severe numerical challenges when attempting to perform simulations with the RSF parameters derived from Fig. 4. To remedy this, we have repeated the steady-state simulations for a lower value of the geometric factor $H = 0.2$ (Fig. 5). This effectively reduces the magnitude of $(a - b)$ (Fig. 5c) and increases the magnitude of D_c (Fig. 5d). Furthermore, H strongly controls the rate of slip weakening in response to an instantaneous velocity-step, and therefore affects the frictional stability of the fault (see Appendix B, Eq. (B.5)). As mentioned earlier, the values of H and ϕ_c are at present not tightly constrained for grain size distributions typical for fault gouges (e.g. power-law or log-normal; Marone and Scholz, 1989; Storti et al., 2003). Furthermore, H and ϕ_c are expected to decrease with increasing phyllosilicate content, by lowering the dilatancy involved in granular flow and by more efficient occupation of the pore space. It has been shown in laboratory experiments that the presence of a continuous mineral foliation effectively raises $(a - b)$ (Collettini et al., 2011), consistent with our interpretation of tanψ. We will use the equivalent RSF parameters derived from the steady-state simulations exhibiting $H = 0.2$ to perform the RSF simulation, which is subsequently compared with the native CNS simulation for which $H = 0.2$. Then the CNS simulation with $H = 0.2$ will be compared with a CNS simulation with $H = 0.5$ (other parameters remaining constant) to evaluate the role played by H. We would like to stress the point that H and ϕ_c are purely geometrical parameters, and we anticipate no depth-dependence of these parameters in the absence of grain comminution and poro-elastic effects.

In contrast with the brittle region, the 'ductile' (steady-state) velocity-strengthening region (below 10 km depth), shows practically no variation in the microstructural state (i.e. porosity), and the velocity-step data is best represented by $b = 0$. By doing so, D_c becomes undefined, and is inconsequentially assumed to remain constant. In the ductile region of the crust, fault slip is predominantly accommodated by pressure solution creep ($\dot{\gamma}_{gr} \ll \dot{\gamma}_{ps}$ so that $V \approx L\dot{\gamma}_{ps}$), which, in the adopted formulation, acts as a linearly viscous fluid. Ignoring any contributions from state evolution ($b \approx 0$ or equivalently ϕ remaining constant near ϕ_0), the fault shear strength in this regime can be obtained directly from rewriting Eq. (4a), which yields:

$$\tau \approx \frac{RTd}{AI_s\Omega}\frac{V}{L} \tag{15}$$

Then, by definition of $a = \partial\mu/\partial\ln(V)$ (Rice et al., 2001), we obtain that in the ductile regime $a = \tau/\sigma$, which is supported by the comparison of the profiles of τ/σ and a in Fig. 4b and c.

Finally, the characteristic slip distance D_c is observed to vary within one order of magnitude over the entire depth range for which it could be determined. Its magnitude is significantly larger than typical laboratory measurements (commonly of the order of tens of μm; Marone et al., 1990), which is directly related to the chosen thickness of the fault zone L: D_c as derived by Chen et al. (2017) is proportional to L (as was also demonstrated experimentally by Marone and Kilgore, 1993). The value of L is chosen in this study to be constant at 1 cm, which is in the range of commonly reported values for cataclasite-rich principal slip zones (e.g. Demurtas et al., 2016; Smeraglia et al., 2017), although we cannot exclude the possibility that the thickness of the fault zone (or more precisely: the degree of localisation), evolves during the seismic cycle.

4.2. Transient fault slip behaviour

The transient behaviour, i.e. the evolution of fault slip velocity during the seismic cycle, is investigated as described in Section 3.2. The spatio-temporal distribution of accumulated fault slip of the CNS simulation with $H = 0.5$ is presented in Fig. 6. In this figure, contours of fault slip are plotted at fixed temporal intervals, which are based on the maximum slip velocity V_{max} recorded over the entire fault at each given time interval. The blue contours represent slow, interseismic creep ($V_{max} < 10^{-7}$ m/s), and are spaced every 5 years. The green contours represent subseismic (nucleation or postseismic) velocities ($10^{-7} < V_{max} < 10^{-2}$ m/s), and are spaced every 0.1 days. Finally, the coseismic stage ($V_{max} > 10^{-2}$ m/s) is represented by the red contours, which are spaced every 2 s. The slip contours are relative to the slip distribution achieved at the end of the first seismic event, which is not shown in Fig. 6.

In the CNS simulation, small slow slip events nucleate at shallow depths (2-3 km) that propagate down and produce stress concentrations. Once sufficient stress has been accumulated, the nucleation of a seismic event initiates at a depth of 3 km, and expands in the down-dip direction. At a depth of 6 km, the fault reaches coseismic velocities and continues to dynamically propagate down to a depth of about 11 km. The highest slip velocities are attained at depths greater than 8 km,

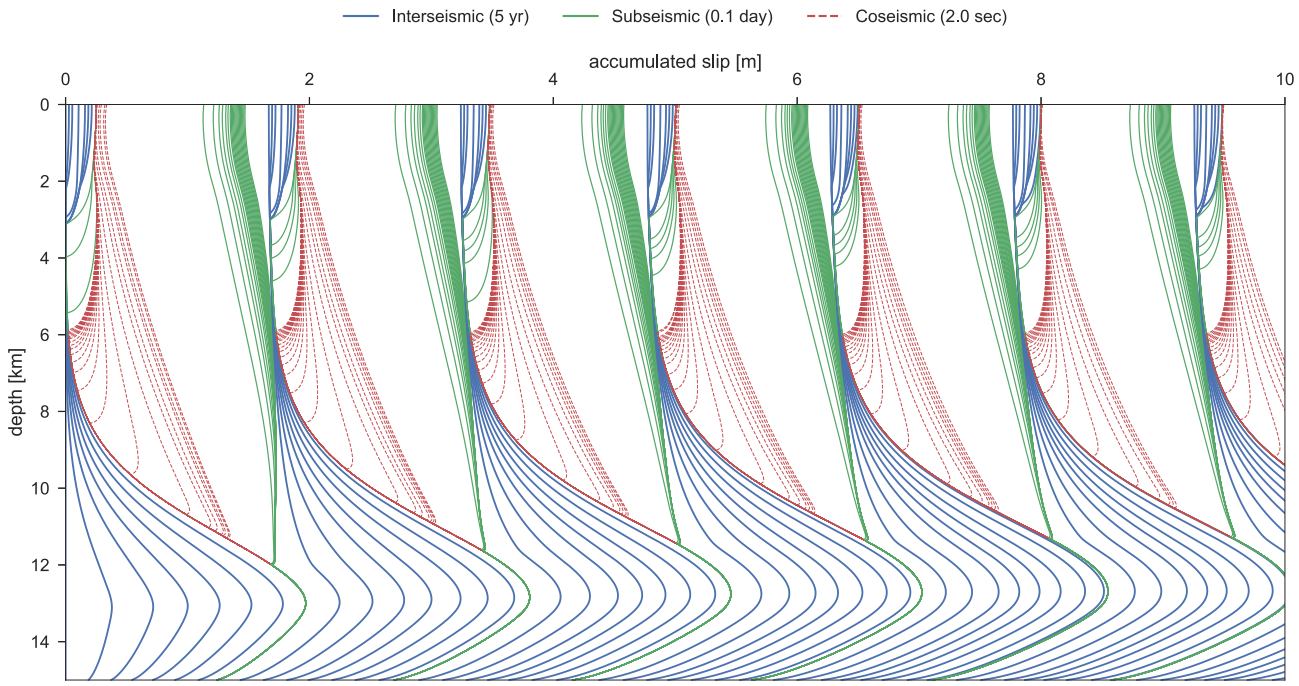

Fig. 6. Spatio-temporal evolution of fault slip from the CNS simulation with $H = 0.5$, relative to the slip distribution after the first seismic event. Contours of fault slip are plotted at fixed temporal intervals based on the maximum slip velocity recorded on the fault. The blue contours represent slow, interseismic creep ($V_{max} < 10^{-7}$ m/s), and are spaced every 5 years. The green contours represent subseismic (nucleation or postseismic) velocities ($10^{-7} < V_{max} < 10^{-2}$ m/s), and are spaced every 0.1 days. The coseismic stage ($V_{max} > 10^{-2}$ m/s) is represented by the red contours, which are spaced every 2 s. See legend for colour-coding and temporal spacing of the slip contours. (For interpretation of the references to color in this figure legend, the reader is referred to the web version of this article.)

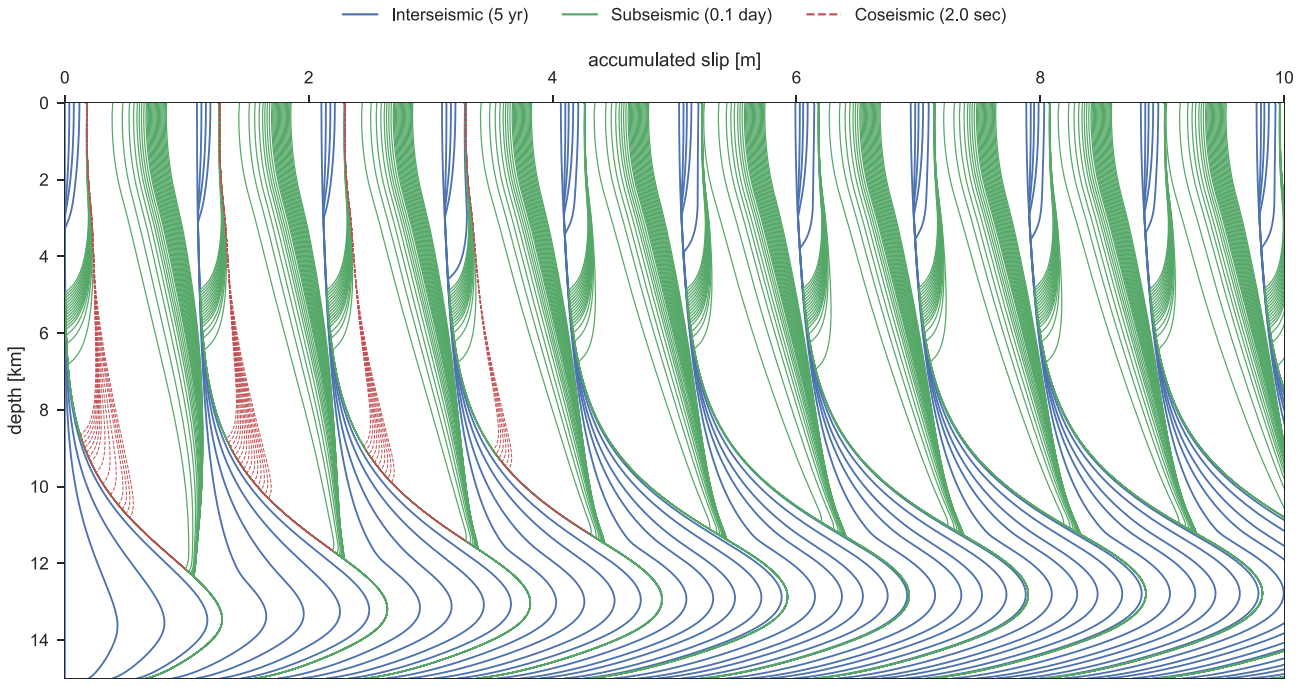

Fig. 7. Spatio-temporal evolution of fault slip from the CNS simulation with $H = 0.2$, relative to the slip distribution after the first seismic event. Contours of fault slip are plotted at fixed temporal intervals based on the maximum slip velocity recorded on the fault. The blue contours represent slow, interseismic creep ($V_{max} < 10^{-7}$ m/s), and are spaced every 5 years. The green contours represent subseismic (nucleation or postseismic) velocities ($10^{-7} < V_{max} < 10^{-2}$ m/s), and are spaced every 0.1 days. The coseismic stage ($V_{max} > 10^{-2}$ m/s) is represented by the red contours, which are spaced every 2 s. See legend for colour-coding and temporal spacing of the slip contours. (For interpretation of the references to color in this figure legend, the reader is referred to the web version of this article.)

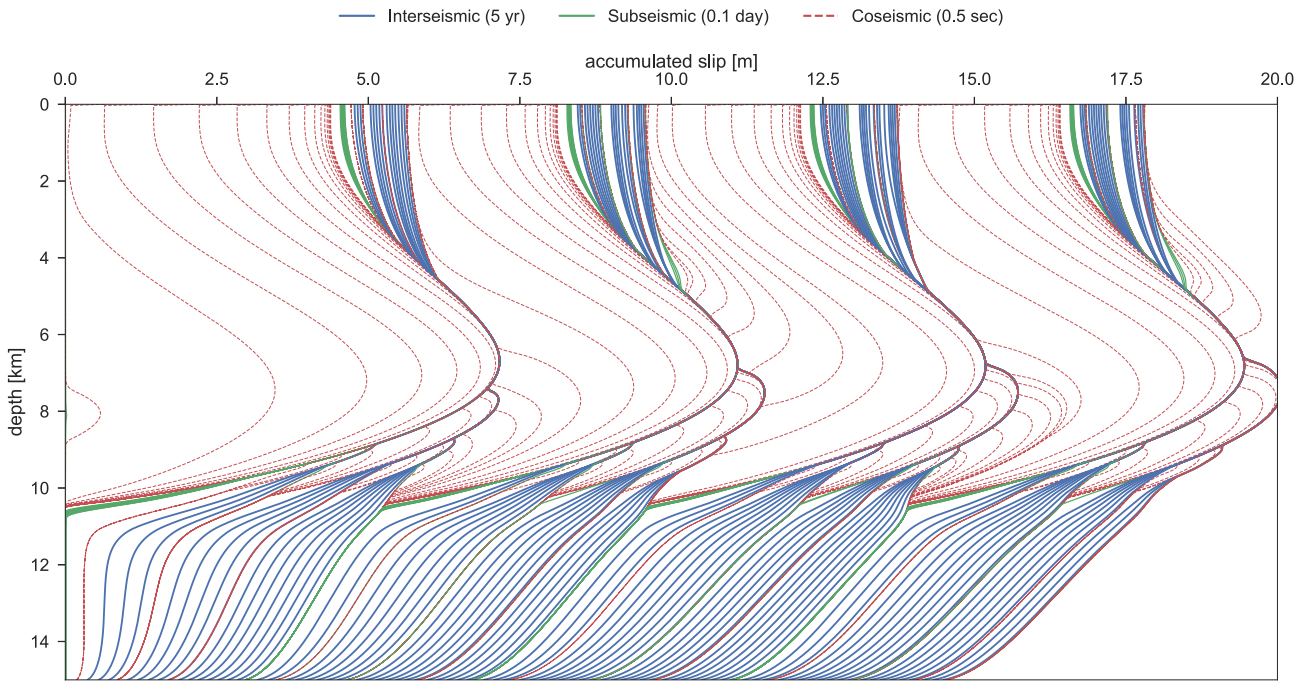

Fig. 8. Spatio-temporal evolution of fault slip from the rate-and-state simulation with the ageing state evolution law, relative to the start of the simulation. Contours of fault slip are plotted at fixed temporal intervals based on the maximum slip velocity recorded on the fault. The blue contours represent slow, interseismic creep ($V_{max} < 10^{-7}$ m/s), and are spaced every 5 years. The green contours represent subseismic (nucleation or postseismic) velocities ($10^{-7} < V_{max} < 10^{-2}$ m/s), and are spaced every 0.1 days. The coseismic stage ($V_{max} > 10^{-2}$ m/s) is represented by the red contours, which are spaced every 0.5 s. See legend for colour-coding and temporal spacing of the slip contours. Note that a different contour interval and horizontal axis are used than in Figs. 6 and 7. (For interpretation of the references to color in this figure legend, the reader is referred to the web version of this article.)

while near the surface slip velocities remain restricted to 0.01 m/s during most events. However, following a seismic event, much of the slip deficit at the surface is relieved by rapid afterslip (as indicated by the spacing between the last red and first green contour line after each seismic event in Fig. 6). In the simulation with $H = 0.5$, a total of up to 1 m of afterslip is accumulated over a duration of about 1 year, which is in range of geodetical estimates of afterslip (Marone et al., 1991; Perfettini and Avouac, 2007). The total slip accommodated within one seismic cycle is roughly 1.5 m, and so the recurrence time of the seismic events is in the range of 50 years (as also seen in Fig. 9). Note that the fault requires about three seismic cycles to fully settle into a repeating limit cycle.

A somewhat different picture emerges when running the same simulation with $H = 0.2$ (Fig. 7). In this simulation, the maximum slip velocity recorded over the entire fault is much lower in value (up to 0.01 m/s), and the imposed deformation within the brittle region is predominantly accommodated by episodic slow slip. The recurrence time between the slow slip events is only about half of the recurrence time seen when $H = 0.5$. Despite this difference, the depth of nucleation, propagation direction, and maximum down-dip extent of the rupture are still comparable between both simulations.

The RSF-based simulations are performed with the equivalent parameters obtained for $H = 0.2$ and $V_{imp} = 10^{-9}$ m/s, and so the RSF results presented in Fig. 8 should be compared with the CNS results of Fig. 7. When doing so, we find that the slip behaviour is rather dissimilar from the CNS-based simulations. First of all, the RSF simulation

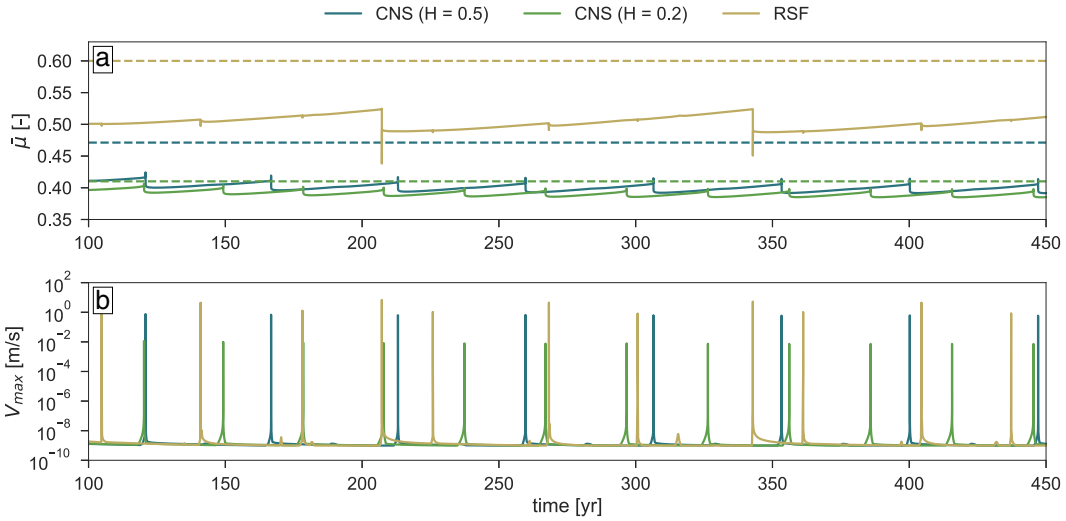

Fig. 9. a) Time-series of the depth-averaged friction coefficient $\bar{\mu}$ at which the fault operates. Solid lines represent the average friction measured during the seismic cycle simulations, dashed lines represent the depth-averaged friction at steady-state ($V = 10^{-9}$ m/s); b) Time-series of the maximum slip velocity V_{max} recorded over the entire fault.

shows large seismic events, producing up to 6 m of coseismic slip in some of the larger events. Additionally, a number of smaller seismic events nucleate at the base of the seismogenic zone (near a depth of 10 km). Within the brittle region, interseismic and postseismic creep are virtually absent, and most of the surface slip is produced at coseismic slip rates. The down-dip extent of the rupture is strongly confined to the boundary with the velocity-strengthening region, and does not traverse this boundary.

The depth-averaged friction at which the fault operates (defined as $\overline{\mu} = \frac{1}{N}\sum \tau_i/\sigma_i$, where N is the number of fault segments), is shown in Fig. 9a. For comparison, the steady-state values of friction, measured at $V = 10^{-9}$ m/s, are indicated by the horizontal dashed lines. Although both the CNS simulations operate at a very similar apparent friction during their respective seismic cycles, their steady-state friction values differ by about 0.06 units of friction. The CNS simulation with $H = 0.2$ operates more closely to its steady-state value than the simulation with $H = 0.5$, or the RSF simulation.

5. Discussion

In the following section, we shall discuss some distinctive features of the various simulations, and make the comparison between them. The discussion will be hosted mostly within a conceptual framework of classical rate-and-state friction, as to build upon previous experience gained from RSF-based studies. Note, however, that the "measured" RSF constitutive parameters are taken as time-constants (i.e. independent of velocity and state), while the equivalent RSF parameters for the CNS model are dependent on e.g. velocity, stress, and porosity (i.e. "state"). This inhibits a one-to-one comparison between the results produced in CNS- and RSF-based simulations, and solicits for the development of a new framework based on microphysical concepts.

5.1. Velocity-dependence of friction

Before discussing the seismic cycle behaviour of the CNS and RSF simulations, we will first discuss the steady-state behaviour of the CNS model. The velocity-dependence of friction as predicted by the CNS model will play a central role in the comparison between the CNS and RSF simulations, and so it would be informative to first point out a number of key features.

Fig. 1 shows the steady-state coefficient of friction and gouge porosity as a function of the imposed velocity, as well as the corresponding values of $(a - b)$, generated with the CNS model parameters for a depth of 6 km and $H = 0.5$. Qualitatively, the shape of these profiles is similar to the depth profiles of μ_{ss} and $(a - b)$ as shown in Fig. 4, with the lowest slip velocities corresponding with the greatest depth or highest temperature, and vice versa. The frictional response of a fault obeying the CNS rheology is the result of the relative rates of granular flow and (thermally-activated) pressure solution creep. Hence, an increase in temperature has a similar effect on the magnitude of μ_{ss} and $(a - b)$ as does a decrease slip velocity, producing similar profiles (see also Niemeijer and Spiers, 2007, their Fig. 10). This trade-off between temperature and velocity has been reported in laboratory studies (Chester and Higgs, 1992; den Hartog et al., 2012; Mitchell et al., 2016; Niemeijer et al., 2016), providing experimental support for the trends in rheology predicted by the CNS model.

It is apparent from Fig. 1b that $(a - b)$ itself is non-monotonically velocity-dependent for any given depth interval. When performing velocity-step tests, either experimentally or numerically (as we have done to obtain the equivalent RSF parameters), a point-measurement is made of the steady-state coefficient of friction and RSF parameters near the given load-point velocity (10^{-9} m/s in our case, but 10^{-6}–10^{-4} m/s are commonly chosen laboratory values). For small deviations from the steady-state velocity, i.e. for small velocity step amplitudes, the values of the obtained $(a - b)$ accurately represent the steady-state velocity-dependence ($d\mu_{ss}/d\ln V$, proportional to the slope of μ_{ss} in Fig. 1a). However, for large deviations, such as attained during the interseismic period ($V \ll V_{imp}$) or during the coseismic phase ($V \gg V_{imp}$), the RSF parameters obtained at V_{imp} no longer capture the rheology of the fault zone. In other words, the tangent line at any point in Fig. 1a is no accurate representation of $(a - b)$ at larger distances from that point, and $(a - b)$ cannot be taken as a constant when considering wide velocity ranges. This feature has been recognised in laboratory experiments (see above references), but is under-appreciated in modelling studies as the velocity-dependence of the RSF parameters is difficult to predict based on laboratory observations alone. The use of a microphysical model facilitates incorporation of this complex velocity-dependence of friction.

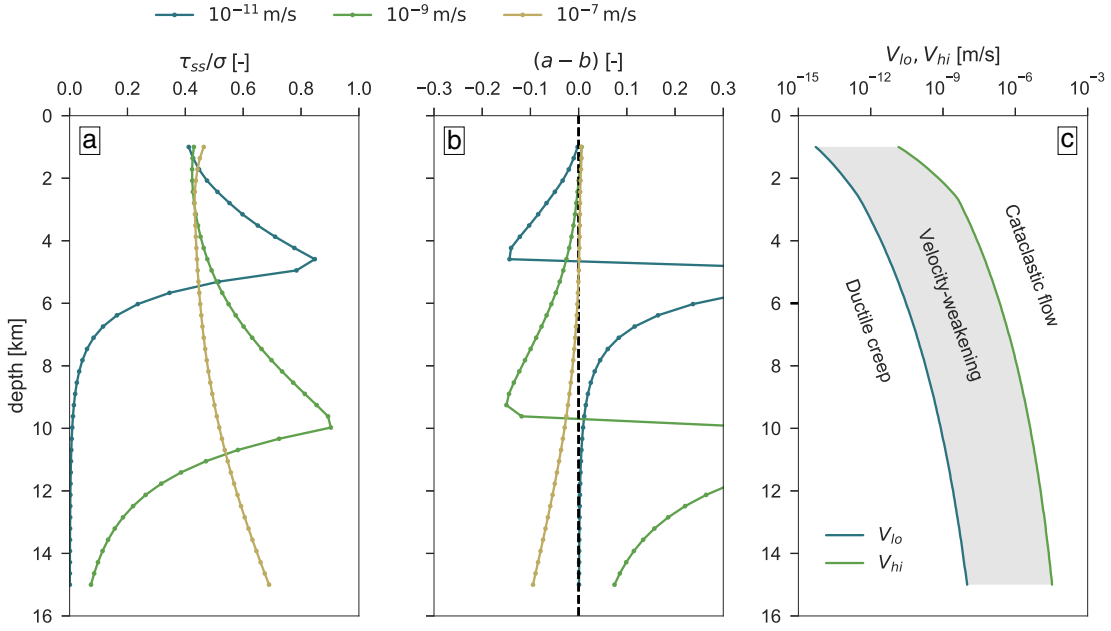

Fig. 10. Steady-state depth-profiles of a) steady-state coefficient of friction, and b) $(a - b)$, generated for imposed velocities of 10^{-11}, 10^{-9} (see legend), and 10^{-7} m/s, and $H = 0.5$. Panel c) shows the transitional velocities V_{lo} and V_{hi}, at which $(a - b) = 0$ (see Fig. 1), deliniatingdelineating the depth-dependence of the three main deformation regimes. (For interpretation of the references to color in this figure, the reader is referred to the web version of this article.)

To illustrate the effect of sliding velocity on the frictional response of our model strike-slip fault, we have re-drawn the steady-state depth profiles of μ_{ss} and $(a-b)$ as shown in Fig. 4 for three different imposed velocities, 10^{-11}, 10^{-9}, and 10^{-7} m/s, see Fig. 10. In this Figure figure, it can be observed that, while the general trends in the profiles of μ_{ss} and $(a-b)$ remain, the region in which $(a-b)$ is at a minimum shifts towards more shallow depths for lower fault slip velocities (and vice versa for higher slip velocities). For the profile of $V = 10^{-7}$ m/s, the transition of velocity-weakening to ductile creep occurs at a depth greater than shown in Fig. 10. The same observation can be made when considering the depth-dependence of the transitional velocities V_{lo} and V_{hi} (Fig. 10c), which delineate the three main deformation regimes. Moreover, during interseismic times, where $V \ll V_{imp}$ for locked fault segments in the seismogenic zone, the fault is expected to deform by ductile creep even in the 'brittle' region at intermediate depths, albeit at $V \ll V_{imp}$. If a given fault segment creeps at a rate lower than V_{lo} (blue line in Fig. 10c), shear stress will increase from the accumulating slip deficit, and so the creep rates increase following Eq. (4a) up to V_{lo}. At slip rates higher than V_{lo}, granular flow is expected to contribute to the total slip velocity, by which the fault enters the velocity-weakening regime at that particular depth, and accelerated slip is anticipated. From a stability perspective, V_{hi} can be considered a stable fixed point, whereas V_{lo} can be considered a half-stable fixed point.

5.2. Comparison of the RSF simulation with previous work

As a brief verification of the numerical method, we qualitatively compare our RSF simulation (based on CNS-derived parameters) with previous work by Lapusta and Rice (2003). In their simulations, values of $(a-b)$ were chosen to have a minimum value of -0.004 in the velocity-weakening region, about one order of magnitude smaller in absolute value than employed in this study ($(a-b) = -0.03$ for $H = 0.2$). Subsequently, the coseismic slip produced by the larger events in Lapusta and Rice (2003) is smaller than presented in this work, which we attribute to the difference in magnitude of $(a-b)$. The parameter values chosen by Lapusta and Rice (2003) were based on the experimental work of Blanpied et al. (1995, 1998) conducted on simulated granite gouges at hydrothermal conditions. The differences between the parameter values measured in the experiments and predicted by the CNS model are substantial, but it should be remarked that the gouge composition (poly-mineralic granite versus mono-mineralic quartz) prevents a direct comparison. Moreover, the observed trends in $(a-b)$ are qualitatively very similar, with a low-temperature velocity-strengthening region, an intermediate-temperature velocity-weakening region, and a very strong velocity-strengthening region at the highest temperatures (Blanpied et al., 1998, their Fig. 7d). Dedicated laboratory tests and model analyses thereof should provide for a more detailed comparison with and validation of the CNS model. As mentioned earlier, the aim of this work is not to accurately simulate the rheology of a particular fault system. Rather, a direct comparison is made between the CNS model implementation and equivalent RSF simulations.

An important finding in the work of Lapusta and Rice (2003) is that for smaller values of D_c (maintaining constant $(a-b)$), the depth of nucleation migrates towards the base of the seismogenic zone, chosen there to lie near 14 km depth. Additionally, smaller magnitude events would nucleate near the base of the seismogenic zone and would produce a non-repetitive sequence of larger and smaller seismic events. The results of Lapusta and Rice (2003) are best interpreted through consideration of a characteristic length scale "L_∞" introduced by Rubin and Ampuero (2005):

$$L_\infty \approx \frac{1}{\pi}\left(\frac{b}{b-a}\right)^2 L_b \tag{16a}$$

$$L_b = \frac{D_c G}{b\sigma} \tag{16b}$$

The use of L_∞ as the characteristic length scale is valid for the ageing state evolution law and with a/b close to but smaller than 1, as adopted in Lapusta and Rice (2003). Smaller values of D_c reduce the magnitude of L_∞, allowing for smaller seismic events to nucleate, in the case of Lapusta and Rice (2003) for a $D_c < 2$ mm. For $a \ll b$, as is the case in the RSF simulation presented in this study, the use of L_b would be more appropriate for a RSF framework in conjunction with the ageing law. In our RSF simulation, the large value of b offsets the relatively large value of D_c (up to 20 mm) to result in a characteristic length scale L_b that is sufficiently small to nucleate minor seismic events, similar to the simulations of Lapusta and Rice (2003).

Apart from the slip displacements achieved during the larger seismic events, the RSF simulation results presented here are qualitatively very similar to those of Lapusta and Rice (2003), and so we will now focus our attention on comparing the RSF simulation with the native CNS simulations.

5.3. Event magnitude and frictional stability

The most apparent difference between the native CNS simulations and the RSF simulation, is that both the maximum slip velocity and slip distance attained during a (sub-)seismic event are much larger in the RSF simulation, even though the relevant RSF parameters have been derived directly from the CNS near-steady state behaviour. This first of all shows that the steady-state behaviour predicted by the CNS model is not directly representative for transient, seismic cycle behaviour. The discrepancies between steady-state and transient behaviour mainly result from the velocity-dependence of the gouge porosity and frictional strength of CNS-controlled faults. At each depth interval, the RSF parameters have been determined near the steady-state velocity V_{imp}. Particularly in the deeper sections of the brittle region (between 8 and 10 km), the estimated values of $(a-b)$ are strongly negative, and represent the maximum rate of velocity-weakening. However, as is apparent from Fig. 1, equivalent values of $(a-b)$ for the CNS model are expected to approach zero and turn positive as the fault accelerates towards coseismic slip velocities, mostly due to a decrease in magnitude of b (Chen et al., 2017). This is in strong contrast with the assumed constant values of a and b in the RSF simulation, which are representative only at $V = 10^{-9}$ m/s. It is expected that as $(a-b)$ approaches zero, the driving potential for accelerating slip vanishes. In other words, the fault stabilises as it accelerates, and so a larger initial potential for a frictional instability (i.e. more negative $(a-b)$, or larger perturbation from steady-state) is required for the development of a seismic event. This is also apparent in the differences between the two CNS simulations: in the initial simulation with $H = 0.5$ and $(a-b)$ in the range of -0.15, seismic slip velocities close to 1 m/s are achieved, whereas in the simulation with $H = 0.2$ and minimum $(a-b) = -0.03$, fault slip velocities do not exceed 0.01 m/s, and the events produced in this simulation would likely be considered slow slip events rather than fast earthquakes.

This transition from velocity-weakening at slow (interseismic) velocities to velocity-strengthening at higher (coseismic) velocities can be effectively simulated by a modified formulation of Eq. (1) (Okubo, 1989):

$$\mu(V,\theta) = \mu^* - a\ln\left(\frac{V_c^*}{V}+1\right) + b\ln\left(\frac{V_c\theta}{D_c}+1\right) \tag{17}$$

where V_c^* and V_c are pre-defined cut-off velocities, so that at $d\mu_{ss}/d\ln(V) = (a-b)$ for $V \ll V_c$, and $d\mu_{ss}/d\ln(V) = a$ for $V_c \ll V \ll V_c^*$. For the purpose of this discussion, the role of V_c^* can be ignored. It has been shown by Shibazaki and Iio (2003) that such a modification facilitates the nucleation and propagation of slow slip transients for appropriate values of V_c. Hence, the small magnitude seismic events and slow slip transients produced in the CNS simulations can indeed be attributed to the transition from velocity-weakening to -strengthening, and is not a

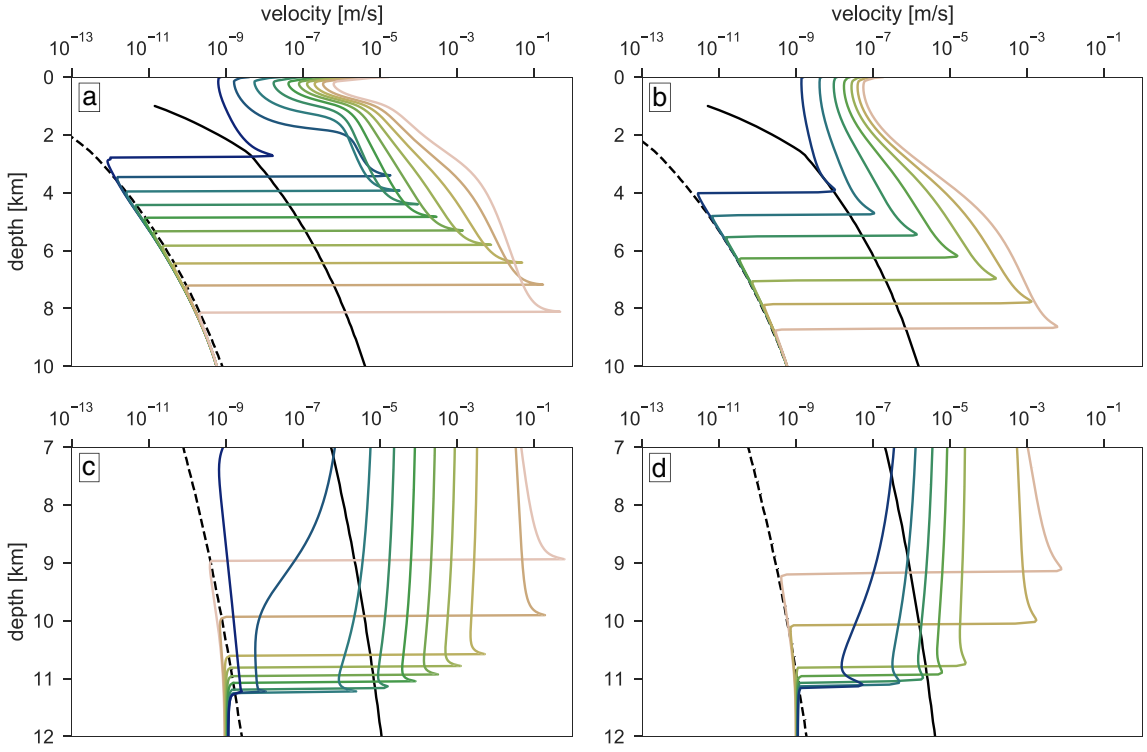

Fig. 11. Snapshots of fault slip velocity versus depth for the fifth event produced in the CNS simulations with $H = 0.5$, and $H = 0.2$. a) and b): Nucleation of the event for $H = 0.5$ and $H = 0.2$, respectively, with snapshots plotted up to the maximum slip velocity attained during the event. The first snapshot is coloured in dark blue, with subsequent snapshots increasing in brightness; c) and d): Arrest of the rupture in the ductile creep region for $H = 0.5$ and $H = 0.2$, respectively, with snapshots plotted from the moment of the maximum slip velocity onwards (subsequent contours are coloured with decreasing brightness); The snapshots are not equally spaced in time, as to clearly visualise both the nucleation, peak velocity, and arrest. The black solid and dashed lines indicate the transitional velocities V_{hi} and V_{lo}, respectively. (For interpretation of the references to color in this figure legend, the reader is referred to the web version of this article.)

unique feature of the adopted fault rheology. This also offers perspectives for studying natural slow slip events using the CNS model formulation, as the transition from velocity-weakening to -strengthening emerges spontaneously from the underlying physical mechanisms.

5.4. Rupture nucleation

In a homogeneously stressed medium, nucleation of a frictional instability is expected to occur near the location of the smallest nucleation length scale (h_{nucl}). In the classical RSF framework with velocity-independent values of a and b, h_{nucl} can be estimated as L_b (Eq. (16b)) for $a \ll b$ (see Eqs. (B.6) and (B.7) in Appendix B). Indeed, from Fig. 8 it is apparent that in the RSF simulation, nucleation of both small and large events occurs near the base of the seismogenic zone, where h_{nucl} assumes its smallest values. However, in the CNS simulation with $H = 0.5$ (Fig. 6), small slow slip events develop at shallow depths ($\sim$ 2 km), with no apparent surface expression. At the depth at which the slow slip events arrest, stress is concentrated and facilitates nucleation of a larger event. In the simulation with $H = 0.2$, the small slow slip events are absent, and nucleation of larger slow slip events initiates at 4 km with no precursory events. The size of the nucleation patch is generally large when compared to the RSF simulation. These observations suggest that near the moment of nucleation, the equivalent value of h_{nucl} is large in magnitude. As discussed in Section 5.3, the equivalent values of D_c, a, and particularly b depend on the instantaneous slip velocity and gouge porosity, and so h_{nucl} can no longer be represented by a constant value of L_b. The reduction of $(a - b)$ with increasing velocity, or more precisely, the reduction of b with increasing porosity cause h_{nucl} to grow, and the nucleation size to increase before coseismic velocities are attained. The slowly accelerating nucleation front in Fig. 6, propagating several kilometres before accelerating dynamically, attests to this. The larger nucleation size also explains the absence of the smaller seismic events in the CNS model, in contrast with the RSF simulation and those of Lapusta and Rice (2003). For a more accurate estimation of the nucleation length scales in the CNS simulations, an in-depth analysis of the fracture energy needs to be performed. We leave this analysis for future study, but a first-order estimate of the fracture energy for a large velocity-step is provided in Appendix B.

A more detailed view of the process of nucleation and arrest of an accelerated slip event is presented in Fig. 11. In this figure, snapshots of fault slip velocity are plotted against a selected depth range for the fifth event produced by the CNS simulations with $H = 0.5$ and $H = 0.2$. These snapshots are spaced at a fixed number of time steps (which are of variable duration, depending on the rate of change of τ and ϕ), rather than at fixed time intervals, in order to clearly visualise the details of the rupture. For reference, the transitional velocities V_{hi} and V_{lo} are plotted as black solid and dashed lines, respectively. In Fig. 11a and b, snapshots of the nucleation process are plotted up to the maximum velocity attained during the event, for $H = 0.5$ and $H = 0.2$, respectively. In Fig. 11c and d, snapshots of the rupture arrest are plotted from the moment of maximum slip velocity up to the moment of arrest, for $H = 0.5$ and $H = 0.2$, respectively. The propagation velocity of the crack tip (V_{prop}) and slip velocity behind the crack tip (V_{max} V_{max}) are plotted in Fig. 12 against the depth at which the crack tip is situated, and as a function of nucleation time ($t_f - t$ where t_f is an arbitrarily chosen moment in time).

Fig. 11a shows that for the CNS simulation with $H = 0.5$, nucleation occurs near the transition of cataclastic flow to velocity-weakening, i.e. near the depth interval where $V_{hi} = V_{imp} = 10^{-9}$. At the moment of nucleation, fault slip at the nucleation front accelerates from 10^{-9} m/s to 10^{-5} m/s over a short depth range of less than 1 km, then decelerates, stabilises, and continues to accelerate at a steady rate (as seen more clearly in Fig. 12a). From thereon, the nucleation zone expands aseismically over a distance of 2 km before reaching coseismic slip

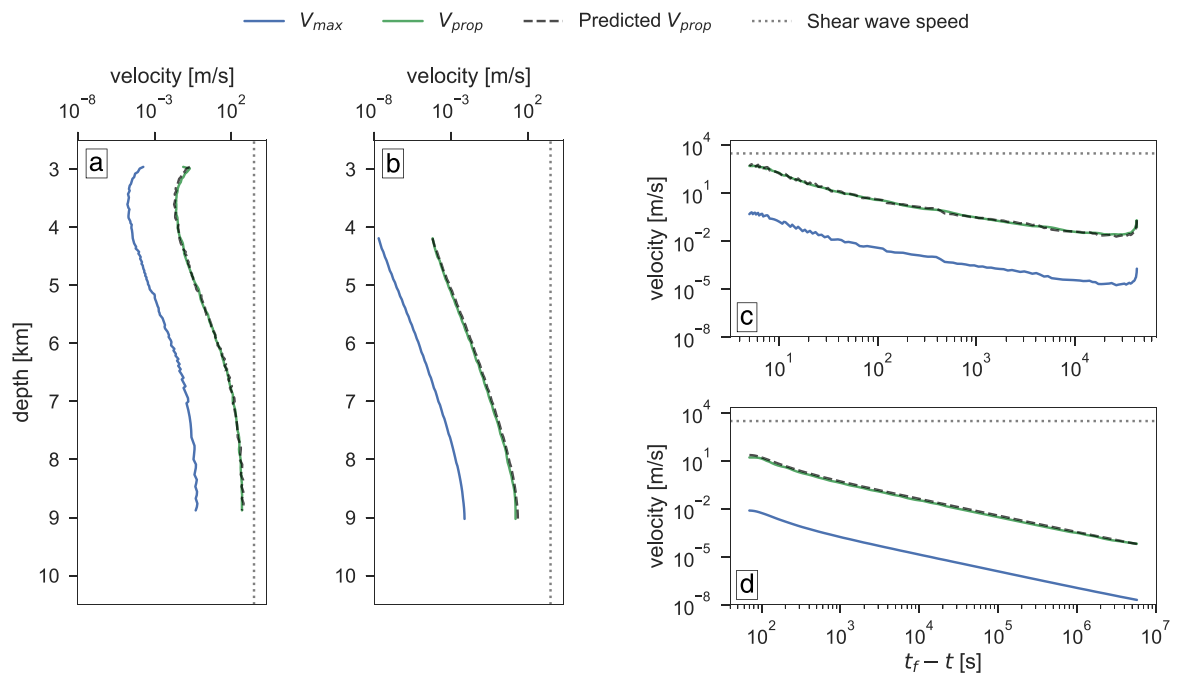

Fig. 12. Recorded slip velocity V_{max} and propapationpropagation velocity V_{prop} at the crack tip, as the rupture front propagates down-dip. Panels a) and c) correspond with Fig. 11a ($H = 0.5$), panels b) and d) correspond with 11c ($H = 0.2$). t_f in panels c) and d) is arbitrarily chosen as to remove non-linearities at small $t_f - t$. The dashed line in each panel represents the predicted V_{prop} based on EquationsEqs. (18) and (21), the gray dotted line indicates the shear wave speed (3000 m/s).

velocities. In the simulation with $H = 0.2$, the initial deceleration is absent, and the acceleration of fault slip is more gentle so that much lower slip velocities are attained (less by two orders of magnitude). Also note that at the moment of nucleation, the majority of the seismogenic (locked) zone creeps at a rate V_{lo} as anticipated in Section 5.1, indicating that the fault is critically stable.

Owing to the coupling with elasticity, the fault slip velocity and down-dip propagation velocity of the rupture tip are interrelated. Following Ida (1973) and Ampuero and Rubin (2008), this relation can accordingly be written as:

$$V_{prop} = \alpha V_{max} \frac{G}{\Delta\tau_{p\text{-}r}} \tag{18}$$

where V_{prop} is the rupture propagation velocity, V_{max} is the maximum slip velocity attained in the near-tip region, α is a shape factor of order 1 (Hawthorne and Rubin, 2013), and $\Delta\tau_{p\text{-}r}$ is the drop in shear stress between the rupture tip ('peak') and the residual stress. Generally, the frictional strength of a fault in the velocity-weakening and cataclastic flow regimes can be described as (Chen and Spiers, 2016):

$$\tau = \frac{\tilde{\mu} + \tan\psi}{1 - \tilde{\mu}\tan\psi}\sigma \tag{19}$$

For a sufficiently long recurrence time in which $\phi \rightarrow \phi_0$, and with negligible porosity evolution ahead of the advancing rupture front, the peak strength of a given fault segment predicted by the CNS model is:

$$\tau_p = \frac{\tilde{\mu}_{\max} + \tan\psi_0}{1 - \tilde{\mu}_{\max}\tan\psi_0}\sigma \tag{20}$$

where $\tilde{\mu}_{\max}$ is the grain-boundary coefficient of friction evaluated at V_{max}, and $\tan\psi_0 = 2H(\phi_c - \phi_0)$. The residual shear strength of the fault is obtained by evaluation of Eq. (19) at the steady-state up-step velocity and porosity. At nucleation slip velocities the porosity behind the rupture tip is approximated by $\phi \approx \phi_c$, so that $\tau_r \approx \tilde{\mu}_{\max}\sigma$. Hence, $\Delta\tau_{p\text{-}r}$ can be estimated as:

$$\Delta\tau_{p\text{-}r} \approx \frac{\tan\psi_0[1 + \tilde{\mu}_{\max}^2]}{1 - \tilde{\mu}_{\max}\tan\psi_0}\sigma \tag{21}$$

Since $\tilde{\mu}$ only has a minor depth- and velocity-dependence (varying by only 0.05 in absolute value over 4 orders of velocity change), the magnitude of $\Delta\tau_{pr}$ is practically constant with depth for the chosen distribution of model parameters ($\tan\psi_0$ and σ are constant below 3 km). By insertion of Eq. (21) into Eq. (18), we obtain a relation between V_{prop} and V_{max}. This relation is tested by comparison with the measured values of V_{max} and V_{prop} for $\alpha = 1$, and is found to provide a near-exact match. In Fig. 12, V_{max} and V_{prop}, as well as the predicted V_{prop} based on Eq. (18), are plotted against depth and against the nucleation time $t_f - t$.

A profound feature of the simulation with $H = 0.5$ (Fig. 12a) is the initial rupture deceleration phase, followed by a brief period of steady propagation of the rupture front. These phases are absent in the simulation with $H = 0.2$ (Fig. 12b), where only acceleration is observed. Similar behaviour has been observed in classical RSF simulations performed by Kaneko and Ampuero (2011), where two converging rupture fronts produced a stress concentration at the point of coalescence, after which nucleation expanded bilaterally. During this second phase of nucleation, the rupture and slip velocities initially decelerated towards a steady rate before accelerating again towards their final values. Likewise, in the simulation with $H = 0.5$, a small slow slip event prior to nucleation of the main event yields a residual stress concentration upon arrest. The main event then nucleates from this perturbation, resulting in a phase of deceleration and steady slip similar to the observations of Kaneko and Ampuero (2011). These authors also provide a theoretical basis for the observed behaviour based on fracture mechanics. In the simulation with $H = 0.2$, no slow slip event and accompanying stress concentration is observed, and the nucleation front accelerates monotonically.

Another interesting result obtained for CNS simulations is the evolution of V_{prop} with the nucleation time $t_f - t$ (Fig. 12c and d). For classical RSF analyses and simulations, it has been found that $V_{prop} \propto (t_f - t)^{-1}$ (e.g. Ampuero and Rubin, 2008; Dieterich, 1992; Noda and Lapusta, 2013). This is observed for both the CNS simulations, as evidenced by the exponent of -1 in the double-logarithmic plots, up to the moment at which the maximum slip velocity is approached. The choice for t_f is arbitrarily made, and is taken here as a free ('fitting')

parameter. However, for the RSF framework, t_f can be expressed in terms of the governing RSF parameters (Rubin and Ampuero, 2005), which in the CNS formulation are dependent on the slip velocity. In spite of this, V_{prop} is still found to be proportional to $(t_f - t)^{-1}$ in the CNS simulations, alluding a more general basis for this feature.

Apart from the initial deceleration phase in the simulation with $H = 0.5$, the nucleation patterns of both CNS simulations are qualitatively very similar, suggesting that the underlying mechanisms for nucleation of slow and fast slip events are similar. In the simulation with $H = 0.5$, the seismogenic zone is sufficiently large for the rupture to propagate dynamically below a depth of 8 km. In the simulation with $H = 0.2$, the nucleation length is likely of similar size as the extent of the seismogenic zone, so that only slow slip events are produced, and the rupture is terminated before the phase of dynamic propagation is reached (Kaneko et al., 2016).

5.5. Rupture arrest

Figs. 1 and 10 also provide insight into the down-dip extent of the rupture in the CNS simulations. In the RSF simulation, the rupture is effectively arrested at the down-dip end of the velocity-weakening region by the large positive value of $(a - b)$, which forms a barrier to accelerated slip. In the CNS formulation, the predicted large values of $(a - b)$ at low velocities (or high temperatures) arise from ductile creep facilitated by pressure solution. In Fig. 1, the regime of ductile creep appears in the velocity range up to $V_{lo} = 5 \times 10^{-11}$ m/s, accompanied by large positive values of $(a - b)$. At intermediate velocities from 10^{-10} to 10^{-8} m/s, the competition between compaction induced by pressure solution and dilatant granular flow results in velocity-weakening behaviour. Hence, a sufficiently large perturbation in velocity or shear stress could trigger a transition from the low-velocity creep regime into the velocity-weakening regime. As a rupture front approaches the down-dip ductile region, the velocity perturbation could render parts of the initially velocity-strengthening region unstable and allow for continued rupture propagation across the brittle-ductile transition. This model prediction is consistent with the findings of pseudotachylyte veins within mylonite zones (e.g. White, 2001), indicating that the dynamic rupture propagated at least partly within ductile creeping regions. Similar results were obtained by Shimamoto and Noda (2014) with an extension of the RSF framework, motivated by laboratory observations to include low-velocity plastic creep and a transition into (frictional) velocity-weakening (Noda and Shimamoto, 2010).

Fig. 11c and d show shows the details of rupture arrest, in which contours of fault slip velocity are plotted against depth. In the CNS simulation with $H = 0.5$ (Fig. 11c), the dynamic rupture decelerates from a depth of 9 km onwards, and is arrested at a depth greater than 11 km. From the steady-state simulations, the brittle-ductile transition is expected to occur near a depth of 10 km, below which deformation is accommodated by steady fault creep at a rate of V_{imp}. In this region, the stress ahead of the rupture can be estimated from Eq. (15). The stress behind the rupture tip can still be approximated as $\tilde{\mu}_{\max}\sigma$, so that the total stress drop is given by:

$$\Delta\tau = \frac{RTd}{AI_s\Omega}\frac{V_{imp}}{L} - \tilde{\mu}_{\max}\sigma \tag{22}$$

Owing to the minor depth- and velocity-dependence of $\tilde{\mu}$, the depth-variation of $\Delta\tau$ in the ductile region is primarily controlled by the kinetics of pressure solution, so that $\Delta\tau$ decreases with depth. Based on fracture mechanics theory, Ampuero et al. (2006) argued that a rupture is arrested when the energy release rate of a crack decreases below the fracture energy. For a steeply decreasing $\Delta\tau(z)$, the depth of rupture arrest roughly equals the depth where $\Delta\tau \leq 0$, which lies at a depth of 11 km in our simulations. Similar reasoning for the down-dip extent of dynamic ruptures was put forward by Brantut and Platt (2017) and Shimamoto and Noda (2014). Since $\Delta\tau$ is independent of H, the same depth of rupture arrest is expected for both of the CNS simulations, as is evident from comparison of Fig. 11b and d. However, the extent of the rupture over which coseismic velocities are maintained likely still depends on H, as the fracture energy for the rupture depends on the magnitude of H. Furthermore, if the steady-state shear strength of the ductile region decays less rapidly with depth (e.g. owing to a lower geothermal gradient, or different deformation mechanisms operating), the extent to which the rupture propagates into the ductile region increases, and the rupture may penetrate a significant distance into regions with $\Delta\tau < 0$ before the energy release rate drops below the fracture energy (Ampuero and Ben-Zion, 2008). Notably, if the shear strength of the ductile region is to remain constant, as would be expected for an along-strike fault segment with no lateral temperature or compositional variations, the ductile velocity-strengthening regions would offer little resistance to the propagation of a dynamic rupture, allowing for continued rupture as long as $\Delta\tau > 0$.

Using a classical RSF numerical framework, Kaneko et al. (2010) investigated the efficiency of rupture arrest of an impeding, velocity-strengthening patch enclosed by two seismogenic, velocity-weakening patches. The authors observed that the probability of a rupture propagating from the first seismogenic patch to the second is strongly related to the resistance offered by the enclosed velocity-strengthening patch. This resistance could be approximated as $C \approx 20\,(a - b)_{vs}\sigma D_{vs}$, with constant $(a - b)_{vs} > 0$, and D_{vs} denoting the length of the patch. The CNS model predicts two distinct regimes of steady-state velocity-strengthening: one ductile creep regime at low velocities $V < V_{lo}$ (or high temperatures), and one high-porosity, cataclastic regime at high velocities $V > V_{hi}$ (or low temperatures; see Fig. 1). In the cataclastic velocity-strengthening regime, $(a - b)$ is mildly increasing with velocity, and so if the velocity-strengthening patch as considered by Kaneko et al. (2010) is interpreted to operate in the cataclastic regime, the conclusions drawn by these authors are expected to be maintained by the CNS model. However, in the geological setting envisioned by Kaneko et al. (2010), i.e. a segment on a subducting plate interface at seismogenic depths, it is more likely that the velocity-weakening patches ('asperities') are embedded as lenses within a low-porosity, ductily or plastically deforming host material (Fagereng and Sibson, 2010; Kimura et al., 2012). As discussed above, a sufficiently large perturbation in either stress or velocity could potentially trigger unstable slip within the velocity-strengthening matrix, facilitating continued rupture even for large positive values of $(a - b)$, as long as the total stress drop $\Delta\tau > 0$. Thus the scaling between the probability of continued rupture, asperity size, and asperity spacing needs to be re-evaluated for a CNS-type rheology. Similar considerations need to be made when dynamic weakening mechanisms operate within inherently velocity-strengthening regions, as was shown by Noda and Lapusta (2013).

5.6. Modes of fault slip

In classical RSF, slow slip transients have successfully been produced in cases where the nucleation length scale was sufficiently large with respect to the fault's spatial dimensions (Hawthorne and Rubin, 2013; Kaneko et al., 2016; Rubin, 2008, see also laboratory evidence by Leeman et al., 2016). In our RSF simulation, where h_{nucl} is particularly small, very little creep is observed outside of the ductile region. In the upper 10 km of the fault, deformation is predominantly accommodated by coseismic slip. This is in strong contrast with the CNS simulations, which feature a mixture of inter-, co-, and postseismic slip on the brittle portion of the fault. Particularly in the CNS simulation with $H = 0.2$, slow slip transients are the dominant mode of slip. This behaviour is readily understood from the velocity-dependence of friction and $(a - b)$ predicted the CNS model (Fig. 1). CNS-governed faults may exhibit a host of deformation modes (ductile creep, stick-slip, and high porosity steady sliding) depending on the instantaneous gouge porosity and rate of deformation. Following a slip event, the porosity on a given section of the fault will be high, which facilitates rapid rates of granular flow and pressure solution, and the fault will deform at a rate $V > V_{imp}$. In

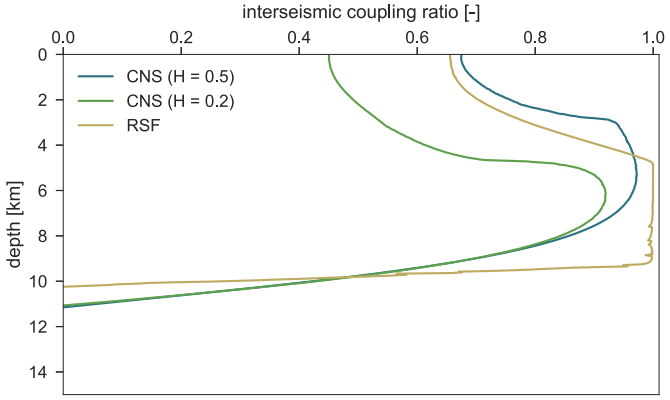

Fig. 13. Depth-profiles of the interseismic coupling ratio (ISC), defined as the cumulative sum of non-interseismic slip $V > 10^{-7}$ m/s over $V_{imp}\Delta t$, for all three simulations. An ISC of 1 indicates full coupling, a value of 0 indicates no coupling.

segments that are identified as velocity-weakening at V_{imp}, the fault strengthens as the gouge densifies and the rate of fault slip diminishes, so that a transition is made back into the velocity-weakening regime where $V < V_{imp}$ (i.e. the fault returns to its 'locked' state). In shallow parts of the crust (e.g. upper 3 km in Fig. 6), no transition is made into the velocity-weakening regime as the porosities remain high owing to much lower compaction rates, and the fault continues to produce creep during the interseismic phase. Over the duration of a seismic cycle, faults may accumulate significant amounts of subseismic slip, even in seismogenic segments.

The degree of coupling of the individual fault segments can be quantified following the definition of interseismic coupling (ISC; Kaneko et al., 2010), which is the ratio of slip deficit accumulated during the interseismic period over the imposed (or long-term) slip $V_{imp}\Delta t$. An ISC value of 1 implies full coupling, i.e. all slip being accommodated by non-interseismic slip, which in our models comprises of both coseismic slip, afterslip, and slip accommodated during nucleation. To be more precise, we define ISC as:

$$\text{ISC} \quad = 1 - \frac{\int V \mathrm{d}t_{int}}{V_{imp}\Delta t} \tag{23}$$

where t_{int} is the interseismic time during which the local slip velocity is less than 10^{-7} m/s. In this way, the value of ISC can be determined for each fault segment individually to produce a depth-profile of ISC (Fig. 13). When comparing the ISC of the RSF simulation with those of the CNS simulations, it becomes apparent that the coupling predicted by the RSF simulation is stronger, and more clearly bounded at the down-dip extent of the locked patch. By contrast, both the CNS simulations show more gradual transitions in their degree of coupling, and generally predict less strong coupling than the RSF simulation. The operation of pressure solution creep in the CNS simulations relieves a portion of accumulated slip deficit within the seismogenic zone, particularly at the down-dip extent of the seismogenic zone (see also Fig. 11a), resulting in lower ISC values. Interestingly, the region of strongest increase in ISC values also coincides roughly with the depth of nucleation of all simulations (at 10 km for the RSF simulation, and at 3 and 5 km for the CNS simulations with $H = 0.5$ and $H = 0.2$, respectively).

As pointed out earlier, the CNS model predicts steady-state, velocity-strengthening fault slip both at very low and high rates of deformation, or alternatively, at low and high temperatures (since the mode of deformation is controlled by the relative rates of $\dot{\gamma}_{gr}$ and temperature-dependent $\dot{\gamma}_{ps}$). This suggests that the presence of steady fault slip at the surface does not necessarily imply low-porosity, ductile creep in a classical sense. Instead, the observed steady creep may well be hosted within high-porosity cataclasites that show little evidence of ductile or crystal plastic deformation mechanisms. The micro-mechanical predictions from the CNS formulation for this regime match the general interpretation of (secondary) 'brittle creep' (Perfettini and Avouac, 2004), i.e. rate-strengthening cataclastic flow, that has previously been analysed in the context of postseismic afterslip and aftershock activity (Marone et al., 1991; Perfettini and Avouac, 2007). In deeper sections of the fault, afterslip and steady creep are accommodated by pressure solution creep, which exhibits a linear viscous rheology at constant (zero) porosity. However, the incorporation of other (high-temperature) creep mechanisms, such as dislocation creep, could result in predominantly power-law rheology at greater depths. For a more in-depth investigation of postseismic creep phenomena, such mechanisms need to be considered, as much evidence points towards a power-law type of rheology operating in the lower crust and upper mantle (e.g. Bürgmann and Dresen, 2008; Montési, 2004).

5.7. The role of dynamic weakening processes and frictional heating

One important feature that is currently absent in both the CNS and RSF simulations employed in this study, is high-velocity dynamic weakening. At high slip velocities and accelerations, heat production by frictional sliding induces numerous thermally-assisted processes, including flash weakening (Rice, 2006), thermochemical pressurisation (Mase and Smith, 1985; Platt et al., 2015), melt lubrication (Hirose and Shimamoto, 2003; Nielsen et al., 2008), and gouge graphitisation (Kuo et al., 2014). Which (combinations) of these mechanisms operate within faults strongly depends on gouge composition and fault zone transport properties, but generally speaking any of these mechanisms has the potential of dramatically reducing the fault's resistance to slip, allowing the fault to operate at extremely low shear stress (Tullis, 2007). It has been shown in several numerical studies that incorporation of dynamic weakening mechanisms strongly affects the magnitude of maximum slip velocity and seismic moment (Noda and Lapusta, 2010, 2013; Thomas et al., 2014). For the case of the CNS simulations presented in this work, it is expected that coseismic slip velocities are intensified by dynamic weakening, possibly producing more coseismic slip at or near the surface (c.f. Noda and Lapusta, 2013).

More importantly, dynamic weakening mechanisms allow the fault to operate at low shear stresses. Recall from Section 5.5 that the maximum down-dip extent of the rupture is controlled by the total stress drop $\Delta\tau$, which reduces to zero as the stress ahead of the rupture decays with depth, while maintaining a near-constant residual strength behind the rupture tip. When the rupture grows to a size that is sufficiently large to attain coseismic velocities, the activation of dynamic weakening induces a larger stress drop and facilitates extended rupture depths (Brantut and Platt, 2017). Continuing this reasoning, a critical length scale for down-dip rupture propagation it is anticipated: when the length scale for nucleation of a dynamic event is of similar size as the extent of the seismogenic zone (as is the case for the CNS simulation with $H = 0.2$), no coseismic velocities are attained before the rupture is arrested in the ductile region. Conversely, when the nucleation length is small enough with respect to the dimensions of the fault, coseismic velocities can be attained and dynamic weakening mechanisms can be triggered, strongly promoting extended rupture. Based on the two CNS simulations presented here, it is expected that this threshold length scale depends on H, rendering the down-dip extent of the rupture sensitive to H (and other parameters that affect h_{nucl}) when dynamic weakening is considered.

In addition to triggering of dynamic weakening mechanisms, frictional heating may further affect the fault rheology by enhancing the rates of pressure solution as a result of a locally perturbed geotherm. For many gouge compositions, an increase in ambient temperature would likely result in enhanced pressure solution creep rates, as the solubility and ionic diffusivity of many materials monotonically increase with temperature (e.g. Dewers and Hajash, 1995; Spiers et al., 2004; van Noort et al., 2008b). Increased pressure solution creep rates may temporarily result in enhanced rates of afterslip. Since the

perturbation of the geotherm is likely confined to the vicinity of the rupture patch, residual stress concentrations at the arrested rupture tip may be relieved by this enhanced creep. One notable exception to this is calcite, which is expected to obey a non-monotonous temperature-dependence of diffusion-controlled pressure solution rates (Verberne et al., 2014; Zhang et al., 2010). Residual heat produced by a seismic event may thus result in a complex spatio-temporal distribution of fault creep and frictional stability of calcite-rich gouges. We leave further investigation into the CNS-governed behaviour of carbonates for future studies.

5.8. Implications and outlook

From simple spring-block analyses, it can be shown that laboratory friction data is well represented by the CNS microphysical model, and that for small-amplitude velocity-step tests the CNS model closely resembles rate-and-state friction transients (Chen and Spiers, 2016). The linearised approximations of the equivalent RSF parameters a, b, and D_c can accurately relate the CNS framework to classical RSF for small perturbations of velocity and state (Chen et al., 2017). The procedure adopted in this study to obtain the equivalent RSF parameters from the CNS model implementation resembles typical laboratory procedures (i.e. velocity-step tests, ideally conducted at in-situ PT-conditions). Still, the resulting transient behaviour produced in the RSF simulation does not correspond to the native CNS model from which the RSF parameters have been derived. This has the following implication for the extrapolation of laboratory results to nature: when laboratory faults that obey CNS-type behaviour (i.e. gouges accommodating deformation by granular flow and pressure solution at appreciable rates) are characterised by classical rate-and-state friction, then the parameters resulting from that characterisation are only accurate at the steady-state sliding velocities that were employed in the laboratory test. At deformation rates and time scales that deviate from the laboratory test conditions, it is likely that the derived parameters no longer describe the transient mechanical response of a fault, and so it is unjustified to use rate-and-state friction as a means for extrapolation of laboratory results to natural scales and conditions.

Instead, using microphysics-based models may offer an alternative for the interpretation of laboratory results, so that the mechanics of natural faults can be represented more accurately. The implementation of microphysical models into (existing) seismic cycle simulators can be used to study the non-steady state behaviour of faults that are heterogeneous in both composition and state of stress. The rheological complexity associated with this new class of numerical models is a requirement for capturing the complexity exhibited by natural fault systems. While the microphysical models pose new challenges, they also offer opportunities for understanding the mechanics of rock friction at a deeper level by connecting laboratory, numerical, and field studies.

6. Conclusions

In this study, we compare the outcomes of seismic cycle simulations that are based on classical rate-and-state friction (RSF) with those based on an implementation of the CNS (*Chen-Niemeijer-Spiers*) microphysical model. From the comparison of the two classes of models, we conclude the following:

- The implementation of the CNS microphysical model is capable of producing seismic cycle transients that have classically been ascribed to rate-and-state friction.
- By simulating laboratory velocity-step tests using the CNS model implementation, the equivalent rate-and-state friction parameters a, b, and D_c can be obtained for near-steady state deformation. However, rate-and-state friction simulations performed with these parameters predict a seismic cycle evolution that is dissimilar from the native CNS model simulations.
- Many of the features of the CNS simulations and differences with the RSF simulation, such as the relatively small event magnitude, the extent of the rupture, and occurrence of slow slip events, can be explained by the predicted velocity-dependence of $(a - b)$. In particular, the transitions between the main deformation regimes play a pivotal role in the rupture nucleation and arrest.
- Owing to the strong velocity-dependence of its rheological properties, we argue that a CNS-governed fault (undergoing deformation by pressure solution and granular flow) cannot be readily described by assumed constant RSF parameters, and that laboratory results of the RSF parameters are only valid for the conditions under which they were obtained.

As is commonly the case, the applicability of the microphysical model employed in this study is bounded by the validity of its assumptions and the quality of the input parameters. However, since this type of models offers a clear physical interpretation of both its assumptions and parameters, firm assessments can be made regarding the accuracy of the model predictions, and dedicated laboratory experiments can be designed to constrain the model parameters to a sufficient degree. Hence, when implemented within numerical frameworks, microphysical models hold potential for improving our understanding of fault rheology and earthquake mechanics through the study of microscale processes.

Acknowledgments

The authors thank the guest editor M.-L. Doah, M. Thomas, and an anonymous reviewer for their thoughtful comments. This project is supported by the European Research Council (ERC), grant no. 335915, and by the NWO Vidi-grant 854.12.001 awarded to A.R. Niemeijer. J.P.A. acknowledges supplemental funding to NSF CAREER grant EAR-1151926 for research opportunities in Europe. The most recent version of the QDYN source code, including the modifications presented in this work, is publicly available at https://github.com/ydluo/qdyn.

Appendix A. Description of the boundary element method

Within our earthquake cycle modelling framework, we presume the existence of a fault with fixed, known geometry that is embedded within a linearly elastic medium. Slip occurs on this prescribed fault surface, and represents the integral of inelastic strain across the width of the fault zone, though the spatial distribution of deformation at a scale smaller than the fault zone width is not explicitly modelled. The mechanics of the fault is only modelled explicitly up to a given depth. In the upper, frictional portion, the fault rheology is governed by a friction law. In the remaining, deeper part of the fault, steady slip is prescribed at a rate V_{imp}, accumulating slip as $d_{imp} = V_{imp} \times t$. This lower 'substrate' of the fault is assumed to extend down into infinity.

To obtain the shear stress at a given point on the frictional part of the fault, we adopt the quasi-dynamic approximation (Rice, 1993):

$$\tau(x, t) = -\mathscr{K}[d - d_{imp}](x, t) - \eta V(x, t) \tag{A.1}$$

The first term on the right hand side represents the static elastic stress induced by slip elsewhere on the fault, which involves a linear functional

$\mathcal{K}[d]$, for which analytical expression are available if the model geometry is simple, e.g. a homogeneous elastic half-space. The second term on the right hand side represents the stress drop due to seismic wave radiation in the direction normal to the fault plane. The parameter η is a damping factor that assumes a value of $G/2c_s$, with G being the shear modulus, and c_s the shear wave speed (Rice, 1993). By employing radiation damping, unbounded limit cycle growth accompanied with unrealistic fault slip velocities is inhibited. The radiation damping representation would be exact if slip were spatially uniform, in which case seismic waves would only be radiated in the direction normal to the fault plane (see Ampuero et al., 2002).

The frictional part of the fault surface is decomposed into a mesh of N non-overlapping elements, and slip is assumed to be uniform inside each element. The following discrete version of Eq. (A.1) is then obtained:

$$\tau_i(t) = -K_{ij}[d_j(t) - d_{imp}] - \eta V_i(t) \tag{A.2}$$

Here, the Einstein summation convention is adopted. The above equation involves the computation of a stress transfer kernel, a matrix whose coefficient K_{ij} represents the shear stress induced on the i-th fault element by a unitary slip on the j-th fault element. The kernel can be computed via existing formulas, e.g. Okada formulas for rectangular elements in a 3D elastic half-space (Okada, 1985). QDYN employs the spectral approach in finite-size domains introduced by Cochard and Rice (1997), together with efficient evaluation of stresses as a convolution via FFT. An alternative form of the equations, more convenient for numerical implementation, is obtained by temporal differentiation of Eq. (A.2):

$$\frac{\mathrm{d}\tau_i}{\mathrm{d}t} = -K_{ij}[V_j(t) - V_{imp}] - \eta\frac{\mathrm{d}V_i(t)}{\mathrm{d}t} \tag{A.3}$$

When the fault rheology is governed by the RSF framework, it is customary to partition $\mathrm{d}\tau_i/\mathrm{d}t$ into partial derivatives with respect to V and θ, so that Eq. (A.3) can be rewritten explicitly for $\mathrm{d}V_i/\mathrm{d}t$. Complemented with a state evolution law (e.g. Eq. (2)) Eq. (2a) and Eq. (2b), this system of ordinary differential equations (ODE) can be rearranged and solved in the form:

$$\frac{\mathrm{d}\mathbf{X}}{\mathrm{d}t} = \mathbf{F}(\mathbf{X}, t) \tag{A.4}$$

where $\mathbf{X}(t)$ is a vector comprising the collection of $V_i(t)$ and $\theta_i(t)$ variables on all fault elements. This system is then solved by a standard, explicit ODE solver with adaptive time stepping. In the CNS model formulation, as described in Section 3.1, it is required to solve for $\tau_i(t)$ rather than $V_i(t)$, and $\theta_i(t)$ is replaced by $\phi_i(t)$, following Eq. (12). The vector $\mathbf{X}(t)$ now contains $\tau_i(t)$ and $\phi_i(t)$, and the local fault slip velocity V_i is calculated as $V_i = L_i(\dot{\gamma}_{gr,i} + \dot{\gamma}_{ps,i})$.

Appendix B. Slip weakening and characteristic length scale

In the classical rate-and-state friction framework, much work focuses on the analysis of characteristic length scales, such as the nucleation length and process zone width (Ampuero and Rubin, 2008; Rice and Ruina, 1983; Rubin and Ampuero, 2005). These are generally obtained by comparison of the fault stiffness with the critical stiffness, or the rate of fault weakening with increasing fault slip. For the derivation of the characteristic length scale for the CNS formulation, we analyse the weakening rate of a fault that accommodates shear strain through granular flow, and that is subjected to an instantaneous velocity-step $V_0 \rightarrow V$ in an infinitely stiff medium.

We first consider the rate of frictional weakening, decomposed into partial derivatives of porosity and velocity:

$$\frac{\mathrm{d}\tau}{\mathrm{d}x} = \frac{1}{V}\left(\frac{\partial\tau}{\partial\phi}\frac{\mathrm{d}\phi}{\mathrm{d}t} + \frac{\partial\tau}{\partial V}\frac{\mathrm{d}V}{\mathrm{d}t}\right) \tag{B.1}$$

For an infinitely stiff medium, $\mathrm{d}V/\mathrm{d}t = 0$. Outside of the ductile creep regime (i.e. $\dot{\gamma}_{gr} \gg \dot{\gamma}_{ps}$), the frictional strength of the fault is given by Chen and Spiers (2016):

$$\tau = \frac{\widetilde{\mu} + \tan\psi}{1 - \widetilde{\mu}\tan\psi}\sigma \tag{B.2}$$

Hence, $\partial\tau/\partial\phi$ can be accordingly written as:

$$\frac{\partial\tau}{\partial\phi} = -2H\sigma\frac{1 + \widetilde{\mu}^2}{(1 - \widetilde{\mu}\tan\psi)^2} \tag{B.3}$$

Combined with Eq. (10b) for $\mathrm{d}\phi/\mathrm{d}t$, the slip weakening rate can now be obtained as:

$$\frac{\mathrm{d}\tau}{\mathrm{d}x} = \frac{2H\sigma}{V}\frac{1 + \widetilde{\mu}^2}{(1 - \widetilde{\mu}\tan\psi)^2}(1 - \phi)\left(\dot{\varepsilon}_{ps} - \tan\psi\frac{V}{L}\right) \tag{B.4}$$

The minimum nucleation length (i.e. fastest weakening rate) is obtained when $\phi \approx 0$, at which point $\dot{\varepsilon}_{ps} \ll \tan\psi V/L$, so that the above relation can be further simplified to:

$$\frac{\mathrm{d}\tau}{\mathrm{d}x} = -\frac{4H^2\phi_c\sigma}{L}\frac{1 + \widetilde{\mu}^2}{(1 - 2\widetilde{\mu}H\phi_c)^2} \tag{B.5}$$

Finally, by equating the critical stiffness k_{cr} to the stiffness of an elastic crack G/h, G being the effective shear modulus and h the crack length, we solve for the minimum crack length h_{cr} which could facilitate a frictional instability:

$$h_{cr} = \frac{GL}{4H^2\phi_c\sigma}\frac{(1 - 2\widetilde{\mu}H\phi_c)^2}{1 + \widetilde{\mu}^2} \tag{B.6}$$

By inserting analytical expressions for b and D_c as given by Chen et al. (2017) into Eq. (B.6), we obtain the familiar result for the crack process zone width (Rubin and Ampuero, 2005):

$$h_{cr} = \frac{D_c G}{b\sigma} = L_b \tag{B.7}$$

For numerically stable simulations, the spatial resolution Δx should be smaller than h_{cr}. In the simulations with $H = 0.5$ and $H = 0.2$, h_{cr} assumes values of 9.1 and 70.8 m, respectively, which are both sufficiently large compared to $\Delta x = 1.8$ m to ensure a well-resolved rupture process zone.

Alternatively, instead of assuming the end-member case for which $\phi = 0$, one could integrate Eq. (10b) over slip distance x to obtain the weakening curve $\tau(x)$, from which the fracture energy can be derived. When we maintain the assumption that $\dot{\varepsilon}_{ps} \ll \tan\psi V/L$, which is valid for $\phi > 0$ when V is relatively high, integration from $\phi(0)$ to ϕ yields:

$$\phi(x) = \frac{\exp\left(-2H\frac{x}{L}[1-\phi_c]\right) - \phi_c\frac{1-\phi(0)}{\phi_c-\phi(0)}}{\exp\left(-2H\frac{x}{L}[1-\phi_c]\right) - \frac{1-\phi(0)}{\phi_c-\phi(0)}} \tag{B.8}$$

Substitution of $\phi(x)$ into Eq. (B.2) gives the evolution of $\tau(x)$, from which the fracture energy G_c can be derived as:

$$\begin{aligned} G_c &= \int_0^\infty [\tau(x) - \tau(\infty)]\mathrm{d}x \\ &= \frac{(1+\widetilde{\mu}^2)L\sigma}{1-2H\widetilde{\mu}(\phi_c-1)} \ln\left(\frac{1-\phi(0)}{1-\phi_c}\frac{1}{1-\widetilde{\mu}\tan\psi_0}\right) \end{aligned} \tag{B.9}$$

where $\tan\psi_0 = 2H(\phi_c - \phi(0))$. The initial condition $\phi(x = 0)$ can be obtained from steady-state solutions (see Chen et al., 2017), although it can be expected that $\phi(0) \approx \phi_0$ for 'locked' seismogenic patches experiencing long interseismic durations. The grain boundary friction coefficient $\widetilde{\mu}$ is evaluated at the up-step velocity, adding a minor velocity-dependent contribution to G_c.

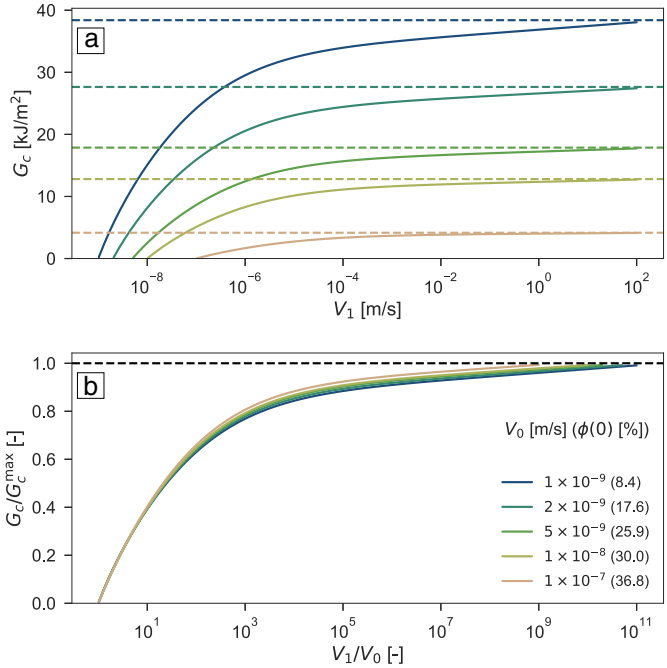

Fig. B.1. The fracture energy G_c predicted for the CNS model, as obtained from numerical integration. a) Magnitude of G_c as a function of the up-step velocity V_1; b) Ratio of G_c to the analytical upper bound G_c^{max} as a function of the velocity-step size V_1/V_0. The analytical upper bounds are plotted as dashed horizontal lines.

Ignoring the operation of pressure solution is mathematically equivalent to assuming that $V \to \infty$. This makes G_c largely independent of V, and only provides an upper bound to the fracture energy. Exact evaluation of G_c for arbitrary velocity-step amplitudes is possible but impractical when no other approximations are made. Instead, we evaluate G_c numerically to get a more accurate estimate. This is done for various initial velocities V_0 and corresponding steady-state porosities $\phi(0)$ (see Fig. B.1). Larger values of V_0 and subsequently $\phi(0)$ are predicted by Eq. (B.9) to result in lower values of the analytical upper bound G_c^{max}. Indeed, from numerical integration we obtain that G_c approaches G_c^{max} for larger magnitudes of the up-step velocity V_1, and that G_c^{max} decreases with increasing $\phi(0)$ (Fig. B.1a).

When the numerically obtained values for G_c are normalised to its corresponding upper bound, and plotted against the magnitude of the velocity-step V_1/V_0, the data converge to a single curve (Fig. B.1b). For small velocity-steps (smaller than a factor of 10), no effect of the initial velocity is apparent. For larger velocity-steps, there is a small but noticeable effect of V_0, with higher initial velocities (and porosities) resulting in a larger G_c/G_c^{max} for a given velocity-step size. The general trends, however, remain.

References

Ampuero, J.P., Ben-Zion, Y., 2008. Cracks, pulses and macroscopic asymmetry of dynamic rupture on a bimaterial interface with velocity-weakening friction. Geophys. J. Int. 173 (2), 674–692. http://dx.doi.org/10.1111/j.1365-246X.2008.03736.x.

Ampuero, J.P., Ripperger, J., Mai, P.M., 2006. Properties of dynamic earthquake ruptures with heterogeneous stress drop. In: Earthquakes: Radiated Energy and the Physics of Faulting. vol. 170. American Geophysical Union, pp. 255–261.

Ampuero, J.P., Rubin, A.M., 2008. Earthquake nucleation on rate and state faults — aging and slip laws. J. Geophys. Res. 113 (B1), B01,302. http://dx.doi.org/10.1029/2007JB005082.

Ampuero, J.P., Vilotte, J.P., Sánchez-Sesma, F.J., 2002. Nucleation of rupture under slip dependent friction law: simple models of fault zone. J. Geophys. Res. Solid Earth 107

(B12). http://dx.doi.org/10.1029/2001JB000452. ESE 2-1-ESE 2-19.
Ariyoshi, K., Matsuzawa, T., Ampuero, J.P., Nakata, R., Hori, T., Kaneda, Y., Hino, R., Hasegawa, A., 2012. Migration process of very low-frequency events based on a chain-reaction model and its application to the detection of preseismic slip for megathrust earthquakes. Earth Planets Space 64 (8), 693–702. http://dx.doi.org/10.5047/eps.2010.09.003.
Beeler, N.M., Hickman, S.H., 2015. Direct measurement of asperity contact growth in quartz at hydrothermal conditions. J. Geophys. Res. Solid Earth 120 (5), 3599–3616. http://dx.doi.org/10.1002/2014JB011816.
Blanpied, M.L., Lockner, D.A., Byerlee, J.D., 1991. Fault Stability Inferred from Granite Sliding Experiments at Hydrothermal Conditions. http://dx.doi.org/10.1029/91GL00469.
Blanpied, M.L., Lockner, D.A., Byerlee, J.D., 1995. Frictional slip of granite at hydrothermal conditions. J. Geophys. Res. 100 (B7), 13,045. http://dx.doi.org/10.1029/95JB00862.
Blanpied, M.L., Marone, C.J., Lockner, D.A., Byerlee, J.D., King, D.P., 1998. Quantitative measure of the variation in fault rheology due to fluid-rock interactions. J. Geophys. Res. 103 (B5), 9691. http://dx.doi.org/10.1029/98JB00162.
Bos, B., Peach, C.J., Spiers, C.J., 2000. Frictional-viscous flow of simulated fault gouge caused by the combined effects of phyllosilicates and pressure solution. Tectonophysics 327.
Bos, B., Spiers, C.J., 2002. Frictional-viscous flow of phyllosilicate-bearing fault rock: microphysical model and implications for crustal strength profiles. J. Geophys. Res. 107.
Boulton, C., Carpenter, B.M., Toy, V., Marone, C., 2012. Physical properties of surface outcrop cataclastic fault rocks, Alpine Fault, New Zealand. Geochem. Geophys. Geosyst. 13 (1). http://dx.doi.org/10.1029/2011GC003872. n/a-n/a.
Boulton, C., Moore, D.E., Lockner, D.A., Toy, V.G., Townend, J., Sutherland, R., 2014. Frictional properties of exhumed fault gouges in DFDP-1 cores, Alpine Fault, New Zealand. Geophys. Res. Lett. 41 (2), 356–362. http://dx.doi.org/10.1002/2013GL058236.
Branch, M.A., Coleman, T.F., Li, Y., 1999. A subspace, interior, and conjugate gradient method for large-scale bound-constrained minimization problems. SIAM J. Sci. Comput. 21 (1), 1–23. http://dx.doi.org/10.1137/S1064827595289108.
Brantut, N., Platt, J.D., 2017. Dynamic Weakening and the Depth Dependence of Earthquake Faulting. In: Thomas, M.Y., Mitchell, T.M., Bhat, H.S. (Eds.), Fault Zone Dynamic Processes: Evolution of 1 Properties During Seismic Rupture, Geophysical Monograph 227. John Wiley & Sons, Inc, pp. 171–194.
Buijze, L., Niemeijer, A.R., Han, R., Shimamoto, T., Spiers, C.J., 2017. Friction properties and deformation mechanisms of halite(-mica) gouges from low to high sliding velocities. Earth Planet. Sci. Lett. 458, 107–119. http://dx.doi.org/10.1016/j.epsl.2016.09.059.
Bürgmann, R., Dresen, G., 2008. Rheology of the lower crust and upper mantle: evidence from rock mechanics, geodesy, and field observations. Annu. Rev. Earth Planet. Sci. 36 (1), 531–567. http://dx.doi.org/10.1146/annurev.earth.36.031207.124326.
Carpenter, B., Collettini, C., Viti, C., Cavallo, A., 2016. The influence of normal stress and sliding velocity on the frictional behaviour of calcite at room temperature: insights from laboratory experiments and microstructural observations. Geophys. J. Int. 205 (1), 548–561. http://dx.doi.org/10.1093/gji/ggw038.
Carpenter, B.M., Marone, C., Saffer, D.M., 2009. Frictional behavior of materials in the 3D SAFOD volume. Geophys. Res. Lett. 36 (5), L05,302. http://dx.doi.org/10.1029/2008GL036660.
Carpenter, B.M., Scuderi, M.M., Collettini, C., Marone, C., 2014. Frictional heterogeneities on carbonate-bearing normal faults: insights from the Monte Maggio Fault, Italy. J. Geophys. Res. Solid Earth 119 (12), 9062–9076. http://dx.doi.org/10.1002/2014JB011337.
Chen, J., Niemeijer, A.R., Spiers, C.J., 2017. Microphysically derived expressions for rate-and-state friction parameters, a, b, and D c. J. Geophys. Res. Solid Earth 122. http://dx.doi.org/10.1002/2017JB014226.
Chen, J., Spiers, C.J., 2016. Rate and state frictional and healing behavior of carbonate fault gouge explained using microphysical model. J. Geophys. Res. Solid Earth 1–42. http://dx.doi.org/10.1002/2016JB013470.
Chester, F.M., 1994. Effects of temperature on friction: constitutive equations and experiments with quartz gouge. J. Geophys. Res. 99 (B4), 7247–7261. http://dx.doi.org/10.1029/93JB03110.
Chester, F.M., Evans, J.P., Biegel, R.L., 1993. Internal structure and weakening mechanisms of the San Andreas Fault. J. Geophys. Res. Solid Earth 98 (B1), 771–786. http://dx.doi.org/10.1029/92JB01866.
Chester, F.M., Higgs, N.G., 1992. Multimechanism friction constitutive model for ultrafine quartz gouge at hypocentral conditions. J. Geophys. Res. Solid Earth 97 (B2), 1859–1870. http://dx.doi.org/10.1029/91JB02349.
Chester, F.M., Logan, J.M., 1987. Composite planar fabric of gouge from the Punchbowl Fault, California. J. Struct. Geol. 9 (5-6). http://dx.doi.org/10.1016/0191-8141(87)90147-7. 621-IN6.
Cochard, A., Rice, J.R., 1997. A spectral method for numerical elastodynamic fracture analysis without spatial replication of the rupture event. J. Mech. Phys. Solids 45 (8), 1393–1418. http://dx.doi.org/10.1016/S0022-5096(97)00004-5.
Collettini, C., Niemeijer, A., Viti, C., Smith, S.A., Marone, C., 2011. Fault structure, frictional properties and mixed-mode fault slip behavior. Earth Planet. Sci. Lett. 311 (3-4), 316–327. http://dx.doi.org/10.1016/j.epsl.2011.09.020.
Demurtas, M., Fondriest, M., Balsamo, F., Clemenzi, L., Storti, F., Bistacchi, A., Di Toro, G., 2016. Structure of a normal seismogenic fault zone in carbonates: the Vado di Corno Fault, Campo Imperatore, Central Apennines (Italy). J. Struct. Geol. 90, 185–206. http://dx.doi.org/10.1016/j.jsg.2016.08.004.
den Hartog, S., Niemeijer, A., Spiers, C., 2012. New constraints on megathrust slip stability under subduction zone P-T conditions. Earth Planet. Sci. Lett. 353-354, 240–252. http://dx.doi.org/10.1016/j.epsl.2012.08.022.
den Hartog, S.A.M., Niemeijer, A.R., Spiers, C.J., 2013. Friction on subduction megathrust faults: beyond the illite-muscovite transition. Earth Planet. Sci. Lett. 373, 8–19. http://dx.doi.org/10.1016/j.epsl.2013.04.036.
den Hartog, S.A.M., Spiers, C.J., 2014. A microphysical model for fault gouge friction applied to subduction megathrusts. J. Geophys. Res. Solid Earth 119 (2), 1510–1529. http://dx.doi.org/10.1002/2013JB010580.
Dewers, T., Hajash, A., 1995. Rate laws for water-assisted compaction and stress-induced water-rock interaction in sandstones. J. Geophys. Res. Solid Earth 100 (B7). http://dx.doi.org/10.1029/95JB00912. 13,093–13,112.
Dieterich, J.H., 1979. Modeling of rock friction: 1. Experimental results and constitutive equations. J. Geophys. Res. 84 (B5), 2161. http://dx.doi.org/10.1029/JB084iB05p02161.
Dieterich, J.H., 1992. Earthquake nucleation on faults with rate- and state-dependent strength. Tectonophysics 211 (1-4), 115–134. http://dx.doi.org/10.1016/0040-1951(92)90055-B.
Dove, P.M., 1999. The dissolution kinetics of quartz in aqueous mixed cation solutions. Geochim. Cosmochim. Acta 63 (22), 3715–3727. http://dx.doi.org/10.1016/S0016-7037(99)00218-5.
Fagereng, A., Sibson, R.H., 2010. Melange rheology and seismic style. Geology 38 (8), 751–754. http://dx.doi.org/10.1130/G30868.1.
Faulkner, D., Lewis, A., Rutter, E., 2003. On the internal structure and mechanics of large strike-slip fault zones: field observations of the Carboneras Fault in southeastern Spain. Tectonophysics 367 (3-4), 235–251. http://dx.doi.org/10.1016/S0040-1951(03)00134-3.
Feucht, L., Logan, J.M., 1990. Effects of chemically active solutions on shearing behavior of a sandstone. Tectonophysics 175 (1-3), 159–176. http://dx.doi.org/10.1016/0040-1951(90)90136-V.
Grauls, D., 1997. Minimum principal stress as control of overpressures in sedimentary basins. In: Hendry, J. (Ed.), Geofluids II '97, pp. 219–222.
Hawthorne, J.C., Rubin, A.M., 2013. Laterally propagating slow slip events in a rate and state friction model with a velocity-weakening to velocity-strengthening transition. J. Geophys. Res. Solid Earth 118 (7), 3785–3808. http://dx.doi.org/10.1002/jgrb.50261.
He, C., Wang, Z., Yao, W., 2007. Frictional sliding of gabbro gouge under hydrothermal conditions. Tectonophysics 445 (3-4), 353–362. http://dx.doi.org/10.1016/j.tecto.2007.09.008.
He, C., Luo, L., Hao, Q.M., Zhou, Y., 2013. Velocity-weakening behavior of plagioclase and pyroxene gouges and stabilizing effect of small amounts of quartz under hydrothermal conditions. J. Geophys. Res. Solid Earth 118 (7), 3408–3430. http://dx.doi.org/10.1002/jgrb.50280.
He, C., Tan, W., Zhang, L., 2016. Comparing dry and wet friction of plagioclase: implication to the mechanism of frictional evolution effect at hydrothermal conditions. J. Geophys. Res. Solid Earth 121 (9), 6365–6383. http://dx.doi.org/10.1002/2016JB012834.
Hickman, S.H., Evans, B., 1991. Experimental pressure solution in halite: the effect of grain/interphase boundary structure. J. Geol. Soc. 148 (3), 549–560. http://dx.doi.org/10.1144/gsjgs.148.3.0549.
Hickman, S.H., Evans, B., 1995. Kinetics of pressure solution at halite-silica interfaces and intergranular clay films. J. Geophys. Res. 100 (B7), 13,113. http://dx.doi.org/10.1029/95JB00911.
Hillers, G., Mai, P.M., Ben-Zion, Y., Ampuero, J.P., 2007. Statistical properties of seismicity of fault zones at different evolutionary stages. Geophys. J. Int. 169 (2), 515–533. http://dx.doi.org/10.1111/j.1365-246X.2006.03275.x.
Hirose, T., Shimamoto, T., 2003. Fractal dimension of molten surfaces as a possible parameter to infer the slip-weakening distance of faults from natural pseudotachylytes. J. Struct. Geol. 25 (10), 1569–1574. http://dx.doi.org/10.1016/S0191-8141(03)00009-9.
Holdsworth, R., van Diggelen, E., Spiers, C., de Bresser, J., Walker, R., Bowen, L., 2011. Fault rocks from the SAFOD core samples: implications for weakening at shallow depths along the San Andreas Fault, California. J. Struct. Geol. 33 (2), 132–144. http://dx.doi.org/10.1016/j.jsg.2010.11.010.
Hunfeld, L.B., Niemeijer, A.R., Spiers, C.J., 2017. Frictional properties of simulated fault gouges from the seismogenic Groningen Gas Field under in-situ P-T-chemical conditions. J. Geophys. Res. Solid Earth 122. http://dx.doi.org/10.1002/2017JB014876.
Ida, Y., 1973. The maximum acceleration of seismic ground motion. Bull. Seismol. Soc. Am. 63 (3), 959–968.
Ikari, M.J., Carpenter, B.M., Marone, C., 2016. A microphysical interpretation of rate-dependent and state-dependent friction for fault gouge. Geochem. Geophys. Geosyst. 16 (8), 2775–2795. http://dx.doi.org/10.1002/2016GC006286.
Iler, R., 1973. Effect of adsorbed alumina on the solubility of amorphous silica in water. J. Colloid Interface Sci. 43 (2), 399–408. http://dx.doi.org/10.1016/0021-9797(73)90386-X.
Imber, J., Holdsworth, R.E., Smith, S.a.F., Jefferies, S.P., Collettini, C., 2008. Frictional-viscous flow, seismicity and the geology of weak faults: a review and future directions. Geol. Soc. Lond., Spec. Publ. 299 (1), 151–173. http://dx.doi.org/10.1144/SP299.10.
Ito, Y., Ikari, M.J., 2015. Velocity- and slip-dependent weakening in simulated fault gouge: implications for multimode fault slip. Geophys. Res. Lett. 42 (21), 9247–9254. http://dx.doi.org/10.1002/2015GL065829.
Kaneko, Y., Ampuero, J.P., 2011. A mechanism for preseismic steady rupture fronts observed in laboratory experiments. Geophys. Res. Lett. 38 (21). http://dx.doi.org/10.1029/2011GL049953. n/a-n/a.
Kaneko, Y., Avouac, J., Lapusta, N., 2010. Towards inferring earthquake patterns from geodetic observations of interseismic coupling. Nat. Geosci. 3 (5), 363–369. http://dx.doi.org/10.1038/ngeo843.

Kaneko, Y., Carpenter, B.M., Nielsen, S.B., 2017. Nucleation process of magnitude 2 repeating earthquakes on the San Andreas Fault predicted by rate-and-state fault models with SAFOD drill core data. Geophys. Res. Lett. 44 (1), 162–173. http://dx.doi.org/10.1002/2016GL071569.

Kaneko, Y., Nielsen, S.B., Carpenter, B.M., 2016. The onset of laboratory earthquakes explained by nucleating rupture on a rate-and-state fault. J. Geophys. Res. Solid Earth 121 (8), 6071–6091. http://dx.doi.org/10.1002/2016JB013143.

Kimura, G., Yamaguchi, A., Hojo, M., Kitamura, Y., Kameda, J., Ujiie, K., Hamada, Y., Hamahashi, M., Hina, S., 2012. Tectonic mélange as fault rock of subduction plate boundary. Tectonophysics 568-569, 25–38. http://dx.doi.org/10.1016/j.tecto.2011.08.025.

Kirkpatrick, J., Rowe, C., White, J., Brodsky, E., 2013. Silica gel formation during fault slip: evidence from the rock record. Geology 41 (9), 1015–1018. http://dx.doi.org/10.1130/G34483.1.

Kuo, L.W., Li, H., Smith, S.A.F., Di Toro, G., Suppe, J., Song, S.R., Nielsen, S., Sheu, H.S., Si, J., 2014. Gouge graphitization and dynamic fault weakening during the 2008 Mw 7.9 Wenchuan earthquake. Geology 42 (1), 47–50. http://dx.doi.org/10.1130/G34862.1.

Lapusta, N., Rice, J.R., 2003. Nucleation and early seismic propagation of small and large events in a crustal earthquake model. J. Geophys. Res. Solid Earth 108 (B4), 1–18. http://dx.doi.org/10.1029/2001JB000793.

Leeman, J., Scuderi, M.M., Marone, C., Saffer, D., 2015. Stiffness evolution of granular layers and the origin of repetitive, slow, stick-slip frictional sliding. Granul. Matter 17 (4), 447–457. http://dx.doi.org/10.1007/s10035-015-0565-1.

Leeman, J.R., Saffer, D.M., Scuderi, M.M., Marone, C., 2016. Laboratory observations of slow earthquakes and the spectrum of tectonic fault slip modes. Nat. Commun. 7 (11), 104. http://dx.doi.org/10.1038/ncomms11104.

Lockner, D.A., Tanaka, H., Ito, H., Ikeda, R., Omura, K., Naka, H., 2009. Geometry of the Nojima Fault at Nojima-Hirabayashi, Japan — I. A simple damage structure inferred from borehole core permeability. Pure Appl. Geophys. 166 (10-11), 1649–1667. http://dx.doi.org/10.1007/s00024-009-0515-0.

Luo, Y., Ampuero, J.P., 2017. Stability and effective friction of faults with heterogeneous friction properties and fluid pressure. Tectonophysics. http://dx.doi.org/10.1016/j.tecto.2017.11.006. (this issue).

Luo, Y., Ampuero, J.P., Miyakoshi, K., Irikura, K., 2017a. Surface rupture effects on earthquake moment-area scaling relations. Pure Appl. Geophys. 174 (9), 3331–3342. http://dx.doi.org/10.1007/s00024-017-1467-4.

Luo, Y., Ampuero, J.P., Galvez, P., Van den Ende, M., Idini, B., 2017b. QDYN: A Quasi-DYNamic Earthquake Simulator (V1.1). http://dx.doi.org/10.5281/zenodo.322459.

Mair, K., Marone, C., 1999. Friction of simulated fault gouge for a wide range of velocities and normal stresses. J. Geophys. Res. Solid Earth 104 (B12). http://dx.doi.org/10.1029/1999JB900279. 28,899–28,914.

Marone, C., Kilgore, B., 1993. Scaling of the critical slip distance for seismic faulting with shear strain in fault zones. Nature 362 (6421), 618–621. http://dx.doi.org/10.1038/362618a0.

Marone, C., Scholz, C.H., 1988. The depth of seismic faulting and the upper transition from stable to unstable slip regimes. Geophys. Res. Lett. 15 (6), 621–624. http://dx.doi.org/10.1029/GL015i006p00621.

Marone, C., Scholz, C.H., 1989. Particle-size distribution and microstructures within simulated fault gouge. J. Struct. Geol. 11 (7), 799–814. http://dx.doi.org/10.1016/0191-8141(89)90099-0.

Marone, C.J., 1998. Laboratory-derived friction laws and their application to seismic faulting. Annu. Rev. Earth Planet. Sci. 26 (1), 643–696. http://dx.doi.org/10.1146/annurev.earth.26.1.643.

Marone, C.J., Raleigh, C.B., Scholz, C.H., 1990. Frictional behavior and constitutive modeling of simulated fault gouge. J. Geophys. Res. 95 (B5), 7007. http://dx.doi.org/10.1029/JB095iB05p07007.

Marone, C.J., Scholtz, C.H., Bilham, R., 1991. On the mechanics of earthquake afterslip. J. Geophys. Res. 96 (B5), 8441. http://dx.doi.org/10.1029/91JB00275.

Mase, C.W., Smith, L., 1985. Pore-fluid pressures and frictional heating on a fault surface. Pure Appl. Geophys. PAGEOPH 122 (2-4), 583–607. http://dx.doi.org/10.1007/BF00874618.

Mitchell, E.K., Fialko, Y., Brown, K.M., 2016. Velocity-weakening behavior of Westerly granite at temperature up to 600 ° C. J. Geophys. Res. Solid Earth 121 (9), 6932–6946. http://dx.doi.org/10.1002/2016JB013081.

Montési, L.G.J., 2004. Controls of shear zone rheology and tectonic loading on post-seismic creep. J. Geophys. Res. Solid Earth 109 (B10). http://dx.doi.org/10.1029/2003JB002925.

Morency, C., Huismans, R.S., Beaumont, C., Fullsack, P., 2007. A numerical model for coupled fluid flow and matrix deformation with applications to disequilibrium compaction and delta stability. J. Geophys. Res. 112 (B10), B10,407. http://dx.doi.org/10.1029/2006JB004701.

Nakatani, M., 2001. Conceptual and physical clarification of rate and state friction: frictional sliding as a thermally activated rheology. J. Geophys. Res. 106 (B7), 13,347. http://dx.doi.org/10.1029/2000JB900453.

Nielsen, S., Di Toro, G., Hirose, T., Shimamoto, T., 2008. Frictional melt and seismic slip. J. Geophys. Res. 113 (B1), B01,308. http://dx.doi.org/10.1029/2007JB005122.

Niemeijer, A., Di Toro, G., Griffith, W.A., Bistacchi, A., Smith, S.A., Nielsen, S., 2012. Inferring earthquake physics and chemistry using an integrated field and laboratory approach. J. Struct. Geol. 39, 2–36. http://dx.doi.org/10.1016/j.jsg.2012.02.018.

Niemeijer, A.R., Boulton, C., Toy, V.G., Townend, J., Sutherland, R., 2016. Large-displacement, hydrothermal frictional properties of DFDP-1 fault rocks, Alpine Fault, New Zealand: implications for deep rupture propagation. J. Geophys. Res. Solid Earth 121 (2), 624–647. http://dx.doi.org/10.1002/2015JB012593.

Niemeijer, A.R., Spiers, C.J., 2002. Compaction creep of quartz-muscovite mixtures at 500 ° C: preliminary results on the influence of muscovite on pressure solution. Geol. Soc. Lond., Spec. Publ. 200 (1), 61–71. http://dx.doi.org/10.1144/GSL.SP.2001.200.01.04.

Niemeijer, A.R., Spiers, C.J., 2006. Velocity dependence of strength and healing behaviour in simulated phyllosilicate-bearing fault gouge. Tectonophysics 427 (1-4), 231–253. http://dx.doi.org/10.1016/j.tecto.2006.03.048.

Niemeijer, A.R., Spiers, C.J., 2007. A microphysical model for strong velocity weakening in phyllosilicate-bearing fault gouges. J. Geophys. Res. 112 (B10), B10,405. http://dx.doi.org/10.1029/2007JB005008.

Niemeijer, A.R., Spiers, C.J., Bos, B., 2002. Compaction creep of quartz sand at 400–600 ° C: experimental evidence for dissolution-controlled pressure solution. Earth Planet. Sci. Lett. 195, 261–275.

Niemeijer, A.R., Vissers, R.L., 2014. Earthquake rupture propagation inferred from the spatial distribution of fault rock frictional properties. Earth Planet. Sci. Lett. 396, 154–164. http://dx.doi.org/10.1016/j.epsl.2014.04.010.

Noda, H., 2008. Frictional constitutive law at intermediate slip rates accounting for flash heating and thermally activated slip process. J. Geophys. Res. Solid Earth 113 (9), 1–12. http://dx.doi.org/10.1029/2007JB005406.

Noda, H., 2016. Implementation into earthquake sequence simulations of a rate- and state-dependent friction law incorporating pressure solution creep. Geophys. J. Int. 205 (2), 1108–1125. http://dx.doi.org/10.1093/gji/ggw058.

Noda, H., Lapusta, N., 2010. Three-dimensional earthquake sequence simulations with evolving temperature and pore pressure due to shear heating: effect of heterogeneous hydraulic diffusivity. J. Geophys. Res. 115 (B12), B12,314. http://dx.doi.org/10.1029/2010JB007780.

Noda, H., Lapusta, N., 2013. Stable creeping fault segments can become destructive as a result of dynamic weakening. Nature 493 (7433), 518–521. http://dx.doi.org/10.1038/nature11703.

Noda, H., Shimamoto, T., 2010. A rate- and state-dependent ductile flow law of polycrystalline halite under large shear strain and implications for transition to brittle deformation. Geophys. Res. Lett. 37 (9). http://dx.doi.org/10.1029/2010GL042512. n/a-n/a.

Noda, H., Shimamoto, T., 2012. Transient behavior and stability analyses of halite shear zones with an empirical rate-and-state friction to flow law. J. Struct. Geol. 38, 234–242. http://dx.doi.org/10.1016/j.jsg.2011.08.012.

Ohtani, T., Fujimoto, K., Ito, H., Tanaka, H., Tomida, N., Higuchi, T., 2000. Fault rocks and past to recent fluid characteristics from the borehole survey of the Nojima Fault ruptured in the 1995 Kobe earthquake, southwest Japan. J. Geophys. Res. Solid Earth 105 (B7). http://dx.doi.org/10.1029/2000JB900086. 16,161–16,171.

Okada, Y., 1985. Surface deformation due to shear and tensile faults in a half-space. Bull. Seismol. Soc. Am. 75 (4), 1135–1154. http://dx.doi.org/10.1016/0148-9062(86)90674-1.

Okubo, P.G., 1989. Dynamic rupture modeling with laboratory-derived constitutive relations. J. Geophys. Res. 94 (B9), 12,321. http://dx.doi.org/10.1029/JB094iB09p12321.

Parry, W., 1998. Fault-fluid compositions from fluid-inclusion observations and solubilities of fracture-sealing minerals. Tectonophysics 290 (1-2), 1–26. http://dx.doi.org/10.1016/S0040-1951(98)00013-4.

Paterson, M.S., 1995. A theory for granular flow accommodated by material transfer via an intergranular fluid. Tectonophysics 245 (3-4), 135–151. http://dx.doi.org/10.1016/0040-1951(94)00231-W.

Perfettini, H., Avouac, J.P., 2004. Postseismic relaxation driven by brittle creep: a possible mechanism to reconcile geodetic measurements and the decay rate of aftershocks, application to the Chi-Chi earthquake, Taiwan. J. Geophys. Res. Solid Earth 109 (B2), 1–15. http://dx.doi.org/10.1029/2003JB002488.

Perfettini, H., Avouac, J.P., 2007. Modeling afterslip and aftershocks following the 1992 Landers earthquake. J. Geophys. Res. 112 (B7), B07,409. http://dx.doi.org/10.1029/2006JB004399.

Perfettini, H., Molinari, A., 2017. A micromechanical model of rate and state friction: 1 static and dynamic sliding. J. Geophys. Res. Solid Earth 122, 2590–2637. http://dx.doi.org/10.1002/2016JB013302.

Platt, J.D., Brantut, N., Rice, J.R., 2015. Strain localization driven by thermal decomposition during seismic shear. J. Geophys. Res. Solid Earth 120, 4405–4433. http://dx.doi.org/10.1002/2014JB011493.

Pluymakers, A.M.H., Spiers, C.J., 2014. Compaction creep of simulated anhydrite fault gouge by pressure solution: theory v. experiments and implications for fault sealing. Geol. Soc. Lond., Spec. Publ. 409 (1), 107–124. http://dx.doi.org/10.1144/SP409.6.

Power, W.L., Tullis, T.E., 1989. The relationship between slickenside surfaces in fine-grained quartz and the seismic cycle. J. Struct. Geol. 11 (7), 879–893. http://dx.doi.org/10.1016/0191-8141(89)90105-3.

Putelat, T., Dawes, J.H.P., Willis, J.R., 2011. On the microphysical foundations of rate-and-state friction. J. Mech. Phys. Solids 59 (5), 1062–1075. http://dx.doi.org/10.1016/j.jmps.2011.02.002.

Reinen, L.A., Tullis, T.E., Weeks, J.D., 1992. Two-mechanism model for frictional sliding of serpentinite. Geophys. Res. Lett. 19 (15), 1535–1538. http://dx.doi.org/10.1029/92GL01388.

Reinen, L.A., Weeks, J.D., 1993. Determination of rock friction constitutive parameters using an iterative least squares inversion method. J. Geophys. Res. 98 (B9), 15,937. http://dx.doi.org/10.1029/93JB00780.

Renard, F., Beauprêtre, S., Voisin, C., Zigone, D., Candela, T., Dysthe, D.K., Gratier, J., 2012. Strength evolution of a reactive frictional interface is controlled by the dynamics of contacts and chemical effects. Earth Planet. Sci. Lett. 344, 20–34. http://dx.doi.org/10.1016/j.epsl.2012.04.048.

Renard, F., Ortoleva, P., Gratier, J.P., 1997. Pressure solution in sandstones: influence of clays and dependence on temperature and stress. Tectonophysics 280 (3-4), 257–266. http://dx.doi.org/10.1016/S0040-1951(97)00039-5.

Rice, J.R., 1992. Fault stress states, pore pressure distributions, and the weakness of the

San Andreas Fault. In: Evans, B., Wong, T.F. (Eds.), Fault Mechanics and Transport Properties of Rocks. Academic Press, pp. 475–503.
Rice, J.R., 1993. Spatio-temporal complexity of slip on a fault. J. Geophys. Res. 98 (B6), 9885. http://dx.doi.org/10.1029/93JB00191.
Rice, J.R., 2006. Heating and weakening of faults during earthquake slip. J. Geophys. Res. Solid Earth 111 (B5). http://dx.doi.org/10.1029/2005JB004006. n/a-n/a.
Rice, J.R., Lapusta, N., Ranjith, K., 2001. Rate and state dependent friction and the stability of sliding between elastically deformable solids. J. Mech. Phys. Solids 49 (9), 1865–1898. http://dx.doi.org/10.1016/S0022-5096(01)00042-4.
Rice, J.R., Ruina, A.L., 1983. Stability of steady frictional slipping. J. Appl. Mech. 50 (2), 343. http://dx.doi.org/10.1115/1.3167042.
Rimstidt, J., Barnes, H., 1980. The kinetics of silica-water reactions. Geochim. Cosmochim. Acta 44 (11), 1683–1699. http://dx.doi.org/10.1016/0016-7037(80)90220-3.
Rimstidt, J.D., 2015. Rate equations for sodium catalyzed quartz dissolution. Geochim. Cosmochim. Acta 167, 195–204. http://dx.doi.org/10.1016/j.gca.2015.07.030.
Rubin, A.M., 2008. Episodic slow slip events and rate-and-state friction. J. Geophys. Res. 113 (B11), B11,414. http://dx.doi.org/10.1029/2008JB005642.
Rubin, A.M., Ampuero, J.P., 2005. Earthquake nucleation on (aging) rate and state faults. J. Geophys. Res. Solid Earth 110 (B11), 1–24. http://dx.doi.org/10.1029/2005JB003686.
Ruina, A., 1983. Slip instability and state variable friction laws. J. Geophys. Res. Solid Earth 88 (B12). http://dx.doi.org/10.1029/JB088iB12p10359. 10,359–10,370.
Saffer, D.M., Marone, C.J., 2003. Comparison of smectite- and illite-rich gouge frictional properties: application to the updip limit of the seismogenic zone along subduction megathrusts. Earth Planet. Sci. Lett. 215 (1-2), 219–235. http://dx.doi.org/10.1016/S0012-821X(03)00424-2.
Sawai, M., Niemeijer, A.R., Plümper, O., Hirose, T., Spiers, C.J., 2016. Nucleation of frictional instability caused by fluid pressurization in subducted blueschist. Geophys. Res. Lett. 43 (6), 2543–2551. http://dx.doi.org/10.1002/2015GL067569.
Scholz, C.H., 2002. The Mechanics of Earthquakes and Faulting. Cambridge University Press, Cambridge. http://dx.doi.org/10.1017/CBO9780511818516.
Schutjens, P.M.T.M., 1991a. Intergranular Pressure Solution in Halite Aggregates and Quartz Sands: An Experimental Investigation. Utrecht University Ph.D. thesis.
Schutjens, P.M.T.M., 1991b. Experimental compaction of quartz sand at low effective stress and temperature conditions. J. Geol. Soc. 148 (3), 527–539. http://dx.doi.org/10.1144/gsjgs.148.3.0527.
Schutjens, P.M.T.M., Spiers, C.J., 1999. Intergranular pressure solution in NaCl: grain-to-grain contact experiments under the optical microscope. Oil Gas Sci. Technol. 54 (6), 729–750. http://dx.doi.org/10.2516/ogst:1999062.
Scuderi, M., Collettini, C., Viti, C., Tinti, E., Marone, C., 2017. Evolution of shear fabric in granular fault gouge from stable sliding to stick slip and implications for fault slip mode. Geology 45 (8). http://dx.doi.org/10.1130/G39033.1. G39,033.1.
Shibazaki, B., Iio, Y., 2003. On the physical mechanism of silent slip events along the deeper part of the seismogenic zone. Geophys. Res. Lett. 30 (9), 1489. http://dx.doi.org/10.1029/2003GL017047.
Shimamoto, T., 1986. Transition between frictional slip and ductile flow for halite shear zones at room temperature. Science 231 (4739), 711–714. http://dx.doi.org/10.1126/science.231.4739.711.
Shimamoto, T., Noda, H., 2014. A friction to flow constitutive law and its application to a 2-D modeling of earthquakes. J. Geophys. Res. Solid Earth 119 (11), 8089–8106. http://dx.doi.org/10.1002/2014JB011170.
Sibson, R.H., 1977. Fault rocks and fault mechanisms. J. Geol. Soc. 133 (3), 191–213. http://dx.doi.org/10.1144/gsjgs.133.3.0191.
Sibson, R.H., 1982. Fault zone models, heat flow, and the depth distribution of earthquakes in the continental crust of the United States. Bull. Seismol. Soc. Am. 72 (1), 151–163.
Sibson, R.H., 1990. Conditions for fault-valve behaviour. Geol. Soc. Lond., Spec. Publ. 54 (1), 15–28. http://dx.doi.org/10.1144/GSL.SP.1990.054.01.02.
Sleep, N.H., 2005. Physical basis of evolution laws for rate and state friction. Geochem. Geophys. Geosyst. 6 (11). http://dx.doi.org/10.1029/2005GC000991. n/a-n/a.
Smeraglia, L., Bettucci, A., Billi, A., Carminati, E., Cavallo, A., Di Toro, G., Natali, M., Passeri, D., Rossi, M., Spagnuolo, E., 2017. Microstructural evidence for seismic and aseismic slips along clay-bearing carbonate faults. J. Geophys. Res. Solid Earth. http://dx.doi.org/10.1002/2017JB014042.
Spiers, C.J., De Meer, S., Niemeijer, A.R., Zhang, X., 2004. Kinetics of rock deformation by pressure solution and the role of thin aqueous films, in Physicochemistry of Water in Geological and Biological Systems. In: Nakashima, S., Spiers, C.J., Mercury, L., Fenter, P.A., Hochella, M.F.J. (Eds.), Universal Academy Press, Tokyo, pp. 129–158.
Storti, F., Billi, A., Salvini, F., 2003. Particle size distributions in natural carbonate fault rocks: insights for non-self-similar cataclasis. Earth Planet. Sci. Lett. 206 (1-2), 173–186. http://dx.doi.org/10.1016/S0012-821X(02)01077-4.
Suppe, J., 2014. Fluid overpressures and strength of the sedimentary upper crust. J. Struct. Geol. 69 (PB), 481–492. http://dx.doi.org/10.1016/j.jsg.2014.07.009.
Takahashi, M., van den Ende, M.P.A., Niemeijer, A.R., Spiers, C.J., 2017. Shear localization in a mature mylonitic rock analog during fast slip. Geochem. Geophys. Geosyst. 18 (2), 513–530. http://dx.doi.org/10.1002/2016GC006687.
Tesei, T., Collettini, C., Barchi, M.R., Carpenter, B.M., Di Stefano, G., 2014. Heterogeneous strength and fault zone complexity of carbonate-bearing thrusts with possible implications for seismicity. Earth Planet. Sci. Lett. 408, 307–318. http://dx.doi.org/10.1016/j.epsl.2014.10.021.
Thomas, M.Y., Lapusta, N., Noda, H., Avouac, J.P., 2014. Quasi-dynamic versus fully dynamic simulations of earthquakes and aseismic slip with and without enhanced coseismic weakening. J. Geophys. Res. Solid Earth 119 (3), 1986–2004. http://dx.doi.org/10.1002/2013JB010615.
Tse, S.T., Rice, J.R., 1986. Crustal earthquake instability in relation to the depth variation of frictional slip properties. J. Geophys. Res. 91 (B9), 9452. http://dx.doi.org/10.1029/JB091iB09p09452.
Tullis, J., Yund, R.A., 1987. Transition from cataclastic flow to dislocation creep of feldspar: mechanisms and microstructures. Geology 15 (7), 606. http://dx.doi.org/10.1130/0091-7613(1987)15<606:TFCFTD>2.0.CO;2.
Tullis, T., 2007. Friction of rock at earthquake slip rates. In: Treatise on Geophysics. vol.4. Elsevier, pp. 131–152.
Urata, Y., Yamashita, F., Fukuyama, E., Noda, H., Mizoguchi, K., 2017. Apparent dependence of rate- and state-dependent friction parameters on loading velocity and cumulative displacement inferred from large-scale biaxial friction experiments. Pure Appl. Geophys. 174 (6), 2217–2237. http://dx.doi.org/10.1007/s00024-016-1422-9.
van der Marck, S.C., 1996. Network approach to void percolation in a pack of unequal spheres. Phys. Rev. Lett. 77 (9), 1785–1788. http://dx.doi.org/10.1103/PhysRevLett.77.1785.
van Noort, R., Visser, H.J.M., Spiers, C.J., 2008a. Influence of grain boundary structure on dissolution controlled pressure solution and retarding effects of grain boundary healing. J. Geophys. Res. 113 (B3), B03,201. http://dx.doi.org/10.1029/2007JB005223.
van Noort, R., Spiers, C.J., Pennock, G.M., 2008b. Compaction of granular quartz under hydrothermal conditions: controlling mechanisms and grain boundary processes. J. Geophys. Res. 113 (B12), B12,206. http://dx.doi.org/10.1029/2008JB005815.
Verberne, B., Chen, J., Niemeijer, A., de Bresser, J., Pennock, G., Drury, M., Spiers, C., 2017. Microscale cavitation as a mechanism for nucleating earthquakes at the base of the seismogenic zone. Nat. Commun. 8. http://dx.doi.org/10.1038/s41467-017-01843-3.
Verberne, B.A., Niemeijer, A.R., De Bresser, J.H.P., Spiers, C.J., 2015. Mechanical behavior and microstructure of simulated calcite fault gouge sheared at 20–600 ° C: implications for natural faults in limestones. J. Geophys. Res. Solid Earth 120 (12), 8169–8196. http://dx.doi.org/10.1002/2015JB012292.
Verberne, B.A., Plümper, O., De Winter, D.A.M., Spiers, C.J., 2014. Superplastic nanofibrous slip zones control seismogenic fault friction. Science 346 (6215), 1342–1344. http://dx.doi.org/10.1126/science.1259003.
Vermeer, P.A., De Borst, R., 1984. Non-associated plasticity for soils, concrete and rock. HERON 29 (3).
White, S., 2001. Textural and microstructural evidence for semi-brittle flow in natural fault rocks with varied mica contents. Int. J. Earth Sci. 90 (1), 14–27. http://dx.doi.org/10.1007/s005310000166.
Zhang, L., He, C., 2016. Frictional properties of phyllosilicate-rich mylonite and conditions for the brittle-ductile transition. J. Geophys. Res. Solid Earth 121 (4), 3017–3047. http://dx.doi.org/10.1002/2015JB012489.
Zhang, X., Spiers, C.J., Peach, C.J., 2010. Compaction creep of wet granular calcite by pressure solution at 28 ° C to 150 ° C. J. Geophys. Res. 115 (B9), B09,217. http://dx.doi.org/10.1029/2008JB005853.
Zheng, G., Rice, J.R., 1998. Conditions under which velocity-weakening friction allows a self-healing versus a cracklike mode of rupture. Bull. Seismol. Soc. Am. 88 (6), 1466–1483.